https://doi.org/10.5194/egusphere-2026-23
Preprint. Discussion started: 15 January 2026
© Author(s) 2026. CC BY 4.0 License.

Refining simulated mineral dust composition through modified size distributions: dual validation with mineral-specific and elemental observations

Sofía Gómez Maqueo Anaya[1], Sudharaj Aryasree[2], Konrad Kandler[2], Eduardo José dos Santos Souza[1], Khanneh Wadinga Fomba[1], Dietrich Althausen[1], Maria Kezoudi[3], Matthias Faust[1], Bernd Heinold[1], Ina Tegen[1], Moritz Haarig[1], Holger Baars[1], and Kerstin Schepanski[4]

[1]Leibniz Institute for Tropospheric Research (TROPOS), Leipzig, Germany
[2]Institute of Applied Geosciences, Technical University of Darmstadt, Germany
[3]Climate and Atmosphere Research Centre (CARE-C), The Cyprus Institute, Nicosia, Cyprus
[4]Free University of Berlin, Berlin, Germany

Correspondence: Sofía Gómez Maqueo Anaya (maqueo@tropos.de)

Abstract. The JATAC2022 campaign in Cape Verde provided a unique opportunity to collect mineral dust aerosols from multiple Saharan source regions and characterize their composition. Mineral dust aerosols comprise a complex assemblage of minerals with distinct physico-chemical properties, leading to differentiated climatic impacts through interactions with radiation, cloud microphysics, and atmospheric chemistry. A crucial physical property governing these interactions is the particle size distribution (PSD), which strongly influences aerosol optical properties, transport, and deposition. Although contemporary atmospheric models have begun integrating mineralogical data into their dust aerosol representations, implementation faces complications due to variations in dust emission parameterizations, making some models more compatible with existing soil mineralogical databases than others.

This work addresses the challenges encountered when incorporating mineralogical information into the COSMO5.05-MUSCAT atmospheric model, which employs a dust emission scheme based on Marticorena and Bergametti (1995). We present an improved approach that refines the translation of mineralogical soil PSDs into emitted aerosol PSDs. The revised implementation is evaluated using historical Saharan dust measurements and new mineralogical observations from the JATAC2022 and DUSTRISK2022 campaigns. Model performance is assessed using a dual validation framework considering both mineral-resolved and elemental composition. The elemental validation approach provides complementary constraints that expose discrepancies in internal mixing assumptions and reveal limitations invisible to mineral-only comparisons. Results indicate that the proposed modification substantially improves representation of phyllosilicates, quartz, and feldspar, while biases in iron, calcium, and magnesium highlight fundamental challenges in representing the heterogeneous internal structure of natural dust particles.

https://doi.org/10.5194/egusphere-2026-23
Preprint. Discussion started: 15 January 2026
© Author(s) 2026. CC BY 4.0 License.

1 Introduction

Mineral dust aerosol is the most abundant atmospheric aerosol type by mass (Kinne et al., 2006) and exerts widespread influence on the Earth system. By scattering and absorbing solar and terrestrial radiation, dust modifies atmospheric heating rates, alters cloud microphysical processes, and perturbs the surface energy balance (Stocker et al., 2013; Kok et al., 2023). Despite this recognized role, large uncertainties remain in quantifying the net radiative forcing by dust. These uncertainties arise from the complex variability of dust properties during emission and transport, including particle size distribution (PSD), morphology, mixing state, and mineralogical composition (Huneeus et al., 2011; Mahowald et al., 2014; Di Biagio et al., 2020).

Mineralogical composition has emerged as a key factor in constraining dust–climate interactions. Different minerals govern how dust interacts with radiation, clouds, and other atmospheric constituents. For instance, small variations in the abundance of iron oxide bearing minerals can strongly amplify shortwave absorption and alter dust's radiative properties (Balkanski et al., 2007; Gómez Maqueo Anaya et al., 2025; Li et al., 2024; Miffre et al., 2023; Obiso et al., 2024; Sokolik and Toon, 1999; Zhang et al., 2024), while silicate minerals differ in their potential to act as ice-nucleating particles (INPs) or cloud condensation nuclei (CCN) under varying conditions (Chatziparaschos et al., 2023; Harrison et al., 2019; Kelly et al., 2007; Murray et al., 2012). Yet, most chemistry transport models treat dust as homogeneous with respect to its composition, neglecting the strong spatial and temporal variability of mineral fractions. This simplification introduces biases in estimates of dust absorption, cloud interactions, and downstream impacts such as nutrient deposition (Kok et al., 2023).

Incorporating mineralogical detail into models is therefore essential, but it depends critically on how the PSD of individual minerals in soils is represented. The PSD controls not only transport and deposition but also the mineral dust particles' interaction with radiation. A central challenge is that the PSD of airborne dust does not directly reflect the PSD of the parent soil: during emission, processes such as soil texture effects, interparticle cohesion, wind friction velocity, and fragmentation and saltation dynamics reshape the particle size distribution (Marticorena and Bergametti, 1995; Kok, 2011). These nonlinear processes lead to size-dependent shifts in mineralogical composition, making the link between soil and atmospheric mineralogy far from trivial.

The particle size distribution of mineral dust fundamentally governs its atmospheric residence time and transport dynamics. Coarse-grained minerals such as quartz, feldspars, and calcite tend to be removed quickly by gravitational settling, resulting in higher concentrations near source regions. In contrast, finer clay-sized phyllosilicates remain suspended for longer periods and thus constitute a major fraction of the dust transported to remote areas (Lawrence and Neff, 2009). The Soil Mineral Atlases (SMAs), a generic term for databases describing the mineralogical composition of soils that are currently employed in atmospheric models, however, classify minerals into only two size fractions, clay (defined as particles with diameters up to 2.5 µm) and silt (particles with diameters between 2.5 to 50 µm), which introduces biases in model simulations. As a result, models tend to overestimate quartz mass fractions in coarser size bins and underestimate them in finer fractions. This discrepancy stems from the assumption of a constant quartz proportion across a wide size range, which does not reflect its reported measured distribution (Kandler et al., 2007, 2009, 2018; Panta et al., 2023).

https://doi.org/10.5194/egusphere-2026-23
Preprint. Discussion started: 15 January 2026
© Author(s) 2026. CC BY 4.0 License.

To address this, some models apply mineral-specific PSD transformations based on the brittle fragmentation theory (BFT) (Kok, 2011), which offers a semi-direct framework for predicting size-resolved emission fluxes of mineral dust particles (e.g., Gonçalves Ageitos et al., 2023; Scanza et al., 2015; Perlwitz et al., 2015a, b). However, many models still rely on emission parameterizations from the scheme developed by Marticorena and Bergametti (1995), which is based on bulk soil properties and cannot directly provide mineral-specific fluxes, particularly given the incomplete mineralogical information in the SMAs commonly used for atmospheric modeling. Assessing the implications of these contrasting approaches is critical for mineral-resolved simulations, yet systematic evaluations remain limited.

In a previous study, Gómez Maqueo Anaya et al. (2024) implemented a mineralogical composition module in Saharan dust simulations within COSMO5.05–MUSCAT. Building on that work, this article addresses a central methodological question: how should the transformation of the particle size distribution (PSD) from soil to atmosphere be represented within the COSMO5.05–MUSCAT dust emission framework to ensure a realistic reproduction of mineralogy-based dust properties? To this end, we evaluate two PSD transformation approaches based on the Marticorena and Bergametti (1995) emission scheme, coupled with the mineralogical database, GMINER (Nickovic et al., 2012). Model results are systematically compared with in-situ measurements of airborne Saharan dust mineralogical composition under different atmospheric transport conditions.

Specifically, we contrast two modeling schemes, hereafter referred to as the 'original' and 'modified' approaches. The 'original' scheme, following Gómez Maqueo Anaya et al. (2024), maps the mineral soil PSD directly onto the aerosol size distribution. While this method adequately represents clay-sized minerals, it shows marked discrepancies for silt-sized fractions when compared with observations. To improve this representation, the 'modified' scheme introduces refinements to the treatment of mineral soil PSD via a redistribution of mineral fractions informed by applications of the BFT, as described in Section 3.2.

The performance of the two schemes is assessed against a compilation of regional North African measurements and concurrent in-situ observations at Cabo Verde from the DUSTRISK (January–February 2022) and Joint Aeolus Tropical Atlantic Campaign (JATAC, June 2022). DUSTRISK provides size-resolved elemental composition, while JATAC offers mineral- and elemental-specific measurements. The observational datasets used for these evaluations are summarized in Section 4.

Through these multi-level comparisons, we evaluate both schemes at the mineral and elemental scales, quantify the impact of the proposed modifications, and explore how seasonal variability (Section 2) in dust source regions influences airborne mineral composition. Results are presented in Section 5.1 for the regional compilation, Section 5.2 for DUSTRISK 2022 campaign, and Section 5.3 for JATAC 2022.

2 Meteorological drivers of dust seasonality

Seasonal variations in meteorological conditions not only control the vertical and horizontal transport of mineral dust but also influence its mineralogical composition by modulating source activation and emission pathways (Kumar et al., 2018). The shifting wind regimes, surface moisture conditions, and boundary-layer dynamics determine which soil types are mobilized and how mineral fractions are mixed during transport. These processes, in turn, shape the composition of dust sampled at

https://doi.org/10.5194/egusphere-2026-23
Preprint. Discussion started: 15 January 2026
© Author(s) 2026. CC BY 4.0 License.

different locations and altitudes. A key contrast in North African dust transport is the altitude of plumes: during the Northern Hemispheric (NH) winter, dust remains largely confined to the lower troposphere, whereas in summer it is frequently lofted into mid-tropospheric layers. These seasonal variations are primarily driven by large-scale shifts in atmospheric circulation patterns over the Sahel and western Sahara (Kalu, 1979; Schepanski et al., 2009).

In NH summer, the northward migration of the Hadley cell shifts the Intertropical Discontinuity (ITD) into the northern Sahel and southern Sahara. The ITD marks the boundary between hot, dry desert air and moist monsoonal inflow from the south. Strong solar heating over the Sahara deepens the planetary boundary layer (PBL), enhancing vertical mixing and dust uplift (Schepanski et al., 2009). At night, an elevated dust layer develops above the monsoonal flow, where geostrophic winds, driven by the pressure gradient between the Saharan Heat Low and the subtropical Atlantic, entrain dust and lift it into the free troposphere (Parker et al., 2005). These elevated plumes are transported westward within the African Easterly Jet and modulated by African Easterly Waves, enabling long-range transport across the Atlantic. Summer dust layers commonly reach altitudes of 5–7 km, facilitating efficient export toward the Caribbean and the Americas (Chiapello et al., 1997; Engelstaedter et al., 2006; Harr et al., 2024).

In contrast, NH winter is characterized by weaker solar heating, a shallower PBL, and a southward retreat of the ITD. Dust sources shift deeper into the southern Sahel, and transport occurs predominantly at lower altitudes (1.5–3 km), carried westward by northeasterly trade winds (Barkan et al., 2004; Chiapello et al., 1997; Kalu, 1979; Harr et al., 2024). This shallow transport regime reduces the vertical extent of plumes, limiting their detectability in satellite retrievals and reducing the likelihood of transatlantic export. This season also coincides with the Sahelian biomass-burning period, during which substantial amounts of anthropogenic aerosols are emitted and frequently mix with the dust layer which complicates remote sensing retrievals of pure dust particles (Gebauer et al., 2025; Heinold et al., 2011; Tesche et al., 2011). Overall, seasonal circulation patterns not only control the altitude and transport pathways of dust but also shape the composition and representativeness of samples collected at receptor sites, such as the Cape Verde archipelago.

3 Methodology

3.1 Model description and parametrizations

The chemistry transport model used in this study is the MUltiScale Chemistry Aerosol Transport (MUSCAT) coupled online with the COnsortium for Small-scale MOdelling (COSMO) v5.05 model. COSMO, developed by the German Weather Service (Deutscher Wetterdienst, DWD), is a non-hydrostatic regional weather prediction model that solves the fundamental equations of atmospheric dynamics on a terrain-following grid (Baldauf et al., 2011). MUSCAT is the online-coupled chemistry transport component, computing the atmospheric transport of aerosols through time-dependent mass balance equations driven by COSMO meteorological fields (Heinold et al., 2011; Wolke et al., 2012). In this work, mineral dust aerosols are represented as passive tracers, i.e., they are not subject to chemical aging or chemically reactive transformations.

The coupled atmosphere-aerosol model system, COSMO-MUSCAT, has been widely applied and evaluated for Saharan dust studies. Previous validation efforts have demonstrated its capability to reproduce dust source activation, transatlantic transport,

https://doi.org/10.5194/egusphere-2026-23
Preprint. Discussion started: 15 January 2026
© Author(s) 2026. CC BY 4.0 License.

and regional dust transport under different meteorological conditions (Heinold et al., 2011; Schepanski et al., 2009; Tegen et al., 2013; Schepanski et al., 2016, 2017). The specific configuration used here has been further evaluated against atmospheric dust loading observations in Gómez Maqueo Anaya et al. (2024) and Gómez Maqueo Anaya et al. (2025).

The atmospheric life cycle of dust aerosols in MUSCAT is represented through a set of physical parameterizations dynamically coupled to COSMO meteorology and updated at every advection step. The main processes include: (1) dust emission, parameterized following Tegen et al. (2002) with modifications to incorporate mineralogical soil fractions as described in Gómez Maqueo Anaya et al. (2024); (2) aerosol transport, solved using a third-order upwind advection scheme with time-splitting integration (Wolke and Knoth, 2000); and (3) aerosol deposition, accounting for both dry and wet removal processes. Dry deposition is parameterized following the formulations of Seinfeld and Pandis (2016) and Zhang et al. (2001), while wet deposition (including in-cloud scavenging or rainout, and below-cloud scavenging or washout) follows the approaches of Berge (1997) and Jakobsen et al. (1997), with detailed implementation described in Heinold et al. (2011).

3.1.1 Dust emission scheme

Dust emission is a non-linear process initiated when near-surface wind velocity generate sufficient vertical shear stress at the soil surface to initiate particle mobilization. In COSMO-MUSCAT, threshold friction velocities are calculated following the parameterization of Marticorena and Bergametti (1995), which accounts for size-resolved soil particle mobilization and depends on soil texture, surface roughness, vegetation, and soil moisture.

Emission fluxes are then computed interactively using the scheme of Tegen et al. (2002), first implemented in COSMO-MUSCAT by Heinold et al. (2007). Fluxes scale with the cube of the wind friction velocity, derived from COSMO-simulated near-surface winds, and are further modulated by vegetation cover and soil moisture. Particle uplift occurs when the effective friction velocity exceeds the size-dependent threshold (U_{t}^{*}), which is controlled by the erodible particle diameter (D_{p}), the aerodynamic roughness length of the total surface (Z_0), and the smoother, erodible fraction roughness length ($z_{0\mathrm{s}}$).

The effective friction velocity is obtained from a drag partitioning approach that reduces the wind's erosive potential by accounting for the sheltering effect of roughness elements. The size-dependent threshold friction velocity is expressed as:

$$U_{\mathrm{t}}^{*}(D_{\mathrm{p}}, Z_0, z_{0\mathrm{s}}) = \frac{U_{\mathrm{ts}}^{*}(D_{\mathrm{p}})}{f_{\mathrm{eff}}(Z_0, z_{0\mathrm{s}})}, \tag{1}$$

where U_{ts}^{*} represents the part of U_{t}^{*} that is available to the erodible soil, called the smooth surface threshold friction velocity, and f_{eff} is the effective drag partition factor:

$$f_{\mathrm{eff}}(Z_0, z_{0\mathrm{s}}) = 1 - \left[\ln\left(\frac{Z_0}{z_{0\mathrm{s}}}\right) / \ln\left(0.35 \left(\frac{10}{z_{0\mathrm{s}}}\right)^{0.8}\right)\right]. \tag{2}$$

For bare desert surfaces, the aerodynamic roughness length (Z_0) is prescribed as 0.001 cm, following the recommendation of Darmenova et al. (2009), while $z_{0\mathrm{s}}$ is obtained from global satellite-derived dataset (Prigent et al., 2005). The smooth-surface threshold friction velocity (U_{ts}^{*}) is estimated from COSMO's 10-meter wind speed output, providing an approximation of the near-surface wind forcing relevant for dust emission.

https://doi.org/10.5194/egusphere-2026-23
Preprint. Discussion started: 15 January 2026
© Author(s) 2026. CC BY 4.0 License.

Dust emission occurs when the surface friction velocity exceeds the size-dependent threshold necessary to mobilize soil particles, provided that soil conditions (e.g., moisture, roughness) are favorable. Once this condition is met, the emitted flux is represented as the horizontal particle flux (G), which scales with the cube of the friction velocity and accounts for the soil particle size distribution:

$$G = \frac{\rho_{\mathrm{a}}}{\mathrm{g}} \cdot U^{*3} \cdot \sum_i \left[\left(1 + \frac{U_{\mathrm{t}}^{*}(D_{\mathrm{pi}}, Z_0, z_{0\mathrm{s}})}{U^{*}}\right) \left(1 - \frac{U_{\mathrm{t}}^{*2}(D_{\mathrm{pi}}, Z_0, z_{0\mathrm{s}})}{U^{*2}}\right) \cdot B_{\text{rel-i}} \right] \text{for } U^{*} \geq U_{\mathrm{t}}^{*}, \tag{3}$$

where ρ_{a} is air density, g is gravitational acceleration, U^{*} is the surface friction velocity, U_{t}^{*} is the threshold friction velocity for each particle diameter (D_{pi}), and $B_{\text{rel-i}}$ represents the relative basal surface area of size fraction i. In MUSCAT, the soil is represented by 196 discrete size fractions ($i = 196$).

Because threshold friction velocity does not scale linearly with particle diameter, an accurate representation of the soil size distribution is required. In the Marticorena and Bergametti (1995) parametrization, the soil particle size distribution (PSD) is modeled using a multi-modal log-normal distribution:

$$\frac{\mathrm{d}m(D_{\mathrm{pi}})}{\mathrm{d}\ln(D_{\mathrm{pi}})} = \sum_{j=1}^{n} \frac{m_j}{\sqrt{2\pi}\ln(\sigma_j)} \exp\left(\frac{\left(\ln D_{\mathrm{pi}} - \ln MMD_j\right)^2}{-2\ln^2\sigma}\right). \tag{4}$$

where j denotes the size mode (clay, silt, sand in the present MUSCAT setup) m_j is the mass fraction of mode j, σ is the geometric standard deviation (set to 2.0 independent of the mode), and MMD_j are the mass median diameters, set to 2.0 µm (clay), 15.0 µm (silt), and 150.0 µm (sand), respectively.

To determine the basal (projected) surface area distribution, the PSD is transformed assuming spherical particles of uniform density:

$$\mathrm{d}B_{\mathrm{t}}(D_{\mathrm{pi}}) = \frac{\mathrm{d}m(D_{\mathrm{pi}})}{\frac{2}{3}\rho D_{\mathrm{pi}}}. \tag{5}$$

The total basal surface area (B_{t}) is obtained by integrating Eq. (5) across all particle sizes. Normalizing $\mathrm{d}B_{\mathrm{t}}(D_{\mathrm{pi}})$ by B_{t} yields the relative basal surface area distribution $B_{\text{rel-i}}$, which is used in Eq. (3) to allocate the horizontal flux across particle sizes.

Saltation and particle bombardment processes (Marticorena and Bergametti, 1995) are incorporated by iteratively adjusting $B_{\text{rel-i}}$ for each size class, accounting for the momentum transfer from saltating particles to finer dust grains. Following this adjustment, the total horizontal flux is computed.

The fraction of the horizontal flux that becomes airborne is parameterized as a vertical dust flux (F):

$$F = \omega \cdot A_{\text{eff}} \cdot G \cdot (1 - A_{\text{snow}}) \cdot I_{\theta}, \tag{6}$$

where ω is the sandblasting efficiency, prescribed per soil type based on the local clay, silt, and sand fractions (Tegen et al., 2002). A_{eff} denotes the erodible surface area, modulated by vegetation cover and aerodynamic roughness, while A_{snow} accounts for the fraction of this area that is snow-covered. The factor I_{θ} represents a soil moisture correction following Fécan et al. (1999).

https://doi.org/10.5194/egusphere-2026-23
Preprint. Discussion started: 15 January 2026
© Author(s) 2026. CC BY 4.0 License.

Table 1. Definition of MUSCAT five independent size classes for mineral dust aerosol transport. Their size limits are indicated.

Bin name	Diameter range
BIN 01	0.2 - 1 µm
BIN 03	1 - 3 µm
BIN 09	3 - 9 µm
BIN 26	9 - 26 µm
BIN 80	26 - 80 µm

The vertical flux is then partitioned into five transport-relevant size bins (Table 1) to generate size-resolved dust fluxes for atmospheric injection. The overall magnitude and spatial variability of emissions are further influenced by surface conditions. Soil moisture reduces emissions linearly above a critical threshold (Fécan et al., 1999), while vegetation cover suppresses fluxes beyond a biome-dependent threshold (0.5 fractional cover in desert regions) and scales them linearly below it (Tegen et al., 2002). Snow cover also inhibits dust emissions; however, its parametrization is deactivated in this model configuration, as its influence over the Sahara Desert is considered negligible. Together with the particle size distribution and surface roughness, these factors control the efficiency and spatial heterogeneity of dust emissions in COSMO-MUSCAT.

3.1.2 Input files and simulation setup

The mineralogical composition simulations in this study were performed using the COSMO5.05-MUSCAT model with a consistent configuration. The only variations among the simulation experiments lie in the time periods considered, some (DUSTRISK) focus on January–February 2022, while for the JATAC 2022 comparisons simulations from June–July 2022 are used. For each of these periods, simulations were performed using two different mineralogical composition approaches, which differences are detailed in the following section.

The COSMO5.05-MUSCAT model domain is set up to cover the majority of the Sahara Desert and extend westward over the Atlantic Ocean to include the Cape Verde archipelago. The domain is bounded by 30.75°W to 39.32°E and 38.49°N to 0.38°S. Simulations are conducted at a horizontal resolution of 0.25° (approximately 28 km), with a vertical discretization of 40 layers. The lowest, surface level, model layer has a thickness of 20 m.

Meteorological initial and boundary conditions for COSMO5.05-MUSCAT are provided by the DWD in the form of 3-hourly meteorological fields. To maintain realistic atmospheric conditions, the model is re-initialized every 48 hours using overlapping cycles. Each 48-hour cycle begins with a 24-hour spin-up phase, during which only the COSMO5.05 meteorological model is active. Following this spin-up, MUSCAT is coupled to COSMO5.05 for the remaining 24 hours to simulate aerosol transport and interactions. Only the output from these second-day simulations, when both COSMO5.05 and MUSCAT are fully coupled, is used for analysis. Continuity between cycles is ensured by starting each new COSMO5.05 run 24 hours prior to the end of the previous MUSCAT simulation, while MUSCAT continues using its own prognostic fields from the preceding cycle as initial conditions.

https://doi.org/10.5194/egusphere-2026-23
Preprint. Discussion started: 15 January 2026
© Author(s) 2026. CC BY 4.0 License.

The MUSCAT dust emission scheme is controlled by external soil-related datasets. Vegetation cover is prescribed using the FCOVER product from the Copernicus Global Land Service (Fuster et al., 2020), which provides fractional green vegetation coverage. Soil moisture input is taken from ERA5-Land hourly reanalysis data (Muñoz Sabater and Copernicus Climate Change Service, 2019), specifically the volumetric soil water content of the uppermost soil layer. Soil texture, expressed in terms of clay, silt, and sand fractions, is provided by the SoilGrids database (Poggio et al., 2021). In addition, the aerodynamic roughness length is prescribed using the dataset by Prigent et al. (2005). Together with the spatial constraints of the model domain, these datasets ensure that only continental dust sources are activated. To evaluate the spatial distribution of active sources, we further use the MSG-SEVIRI dust source activation frequency map by Schepanski et al. (2007).

Mineralogical composition is represented by the GMINER SMA (Nickovic et al., 2012), which was first implemented in the model system by Gómez Maqueo Anaya et al. (2024). The mineralogical fields in GMINER are based on the procedure introduced by Claquin et al. (1999), which identifies dust-productive soils according to the FAO74 classification. Effective mineral fractions are derived by combining soil texture classes, establishing links between soil types and key minerals including quartz, feldspar, calcite, gypsum, illite, kaolinite, smectite, and hematite. Phosphorus, present in several minerals and of particular importance for ocean fertilization, is also included. Mineral and phosphorus fractions are distributed between clay (<2 µm) and silt (2–50 µm) size populations. However, this approach introduces several sources of uncertainty. The relationship between soil type and mineral content is derived from sparse measurements and does not account for regional variability within a soil class. In addition, the underlying measurements are based on wet sedimentation techniques that alter the natural soil composition by breaking aggregates, thereby biasing the mineral allocation toward clay-sized fractions (Perlwitz et al., 2015a). This artifact particularly affects the modeled content of phyllosilicates (illite, kaolinite, and smectite), which observations suggest are more abundant in coarser size ranges (e.g., Kandler et al., 2009). Such uncertainties can lead to large deviations in modeled soil size distributions at emission (Journet et al., 2014; Perlwitz et al., 2015a).

The choice of GMINER as the implemented SMA is motivated by its ability to more accurately reproduce the iron oxide content in the study region (Gonçalves Ageitos et al., 2023). Since the primary objective of this implementation was to assess the impact of iron oxides on lidar-retrieved optical properties (Gómez Maqueo Anaya et al., 2025), GMINER provided a suitable basis for the analysis. At the same time, the comparative study by Gonçalves Ageitos et al. (2023) showed that GMINER also better captures phyllosilicate distributions, particularly kaolinite for North Africa, than the Journet et al. (2014) SMA. Feldspar exhibited greater spatial variability, with lower errors when using GMINER, although feldspar size distributions remain poorly characterized due to their absence from the finer fractions in this dataset. By contrast, calcite concentrations were more accurately represented by Journet et al. (2014), while GMINER systematically underestimated calcite levels over the Sahara Desert. At the time of implementation, these two SMAs were the only datasets available for use.

3.2 Mineralogical composition modification in COSMO5.05-MUSCAT

This section introduces the methodological framework developed to improve and evaluate the representation of mineralogical composition in atmospheric dust simulations. The focus is on modifications to the mineralogical representation in the

https://doi.org/10.5194/egusphere-2026-23
Preprint. Discussion started: 15 January 2026
© Author(s) 2026. CC BY 4.0 License.

COSMO5.05-MUSCAT model (Gómez Maqueo Anaya et al., 2024), designed to enhance how mineral size distributions are treated within simulated aerosol composition.

In the 'original' approach by Gómez Maqueo Anaya et al. (2024), mineralogical fractions are prescribed by directly mapping the mineral soil particle size distribution (PSD) from GMINER (Nickovic et al., 2012) onto the mineral-resolved aerosol PSD (see upper panel of Fig. 2). A key limitation of this approach is that the modifications to the bulk PSD caused by the emission process do not affect the mineral-resolved PSD. This overlooks the fact that the emission process explicitly alters the overall dust PSD, as predicted by dust emission theories (Kok et al., 2012; Marticorena and Bergametti, 1995; Shao et al., 2011).

This inconsistency stems from the structure of GMINER in combination with Marticorena and Bergametti (1995)'s emission scheme, since GMINER provides mineralogical mass fractions only for the finest soil classes (silt and clay). These are assumed to represent the airborne dust range, given their capacity to remain suspended for several days. However, the emission scheme of Marticorena and Bergametti (1995) (Eqs. (3)–(6)) requires the full soil PSD to represent saltation and bombardment processes. Larger soil particles, although not staying airborne, are essential because their impacts release smaller fragments that otherwise could not overcome interparticle cohesion forces (Marticorena and Bergametti, 1995; Iversen and White, 1982).

Consequently, a consistent application of the Marticorena and Bergametti (1995) scheme is not possible with GMINER alone, since the database lacks information on the coarser soil fractions. Figure 1 illustrates this limitation for a representative Saharan grid cell, highlighting the substantial portion of the soil PSD that is missing when mineral fractions are restricted to only the two finest classes.

The emission scheme inherently favors silt-sized particles, which require relatively low wind stress for entrainment and are small enough to remain airborne, as illustrated by the threshold friction velocity curve (in Fig. 1 of Marticorena and Bergametti (1995)). This aerodynamic preference becomes problematic when GMINER assigns minerals exclusively to silt or clay size classes. Treating these mineral-resolved PSDs as representative of the full soil PSD within the Marticorena and Bergametti (1995) framework introduces systematic biases: clay-sized minerals experience artificially suppressed emissions due to high cohesion thresholds that rely on larger saltating particles to be broken, while silt-sized minerals are prone to overestimation in the absence of coarser, non-erodible grains. Accurate dust emission calculations therefore require a complete soil PSD, where larger particles mobilize finer fractions via saltation bombardment (Kok et al., 2012; Marticorena and Bergametti, 1995). This issue is compounded by the methodology used to construct GMINER: wet sieving mechanically disaggregates soil samples, increasing the apparent fraction of clay-sized particles relative to undisturbed soils (Perlwitz et al., 2015a). While airborne clay-sized fractions generally match source soils and are preserved during transport (Caquineau et al., 1998; Lafon et al., 2004), silt-sized mineral distributions show poorer agreement, partly due to biases introduced by wet-sieving (Perlwitz et al., 2015a).

To address these issues, several modeling studies have incorporated mineral-specific transformations from soil to aerosol PSDs (e.g., Perlwitz et al., 2015a, b; Gonçalves Ageitos et al., 2023; Pérez García-Pando et al., 2016; Scanza et al., 2015; Li et al., 2021). These approaches build on the Brittle Fragmentation Theory (BFT) of Kok (2011), which posits that for the finest particles, the emitted size distribution is largely independent of soil properties and wind speed. BFT conceptualizes emission as a sequence of energetic collisions between saltating aggregates, producing fragments that predominantly fall below a characteristic size threshold. The resulting particle number concentration N is inversely proportional to the square of the

https://doi.org/10.5194/egusphere-2026-23
Preprint. Discussion started: 15 January 2026
© Author(s) 2026. CC BY 4.0 License.

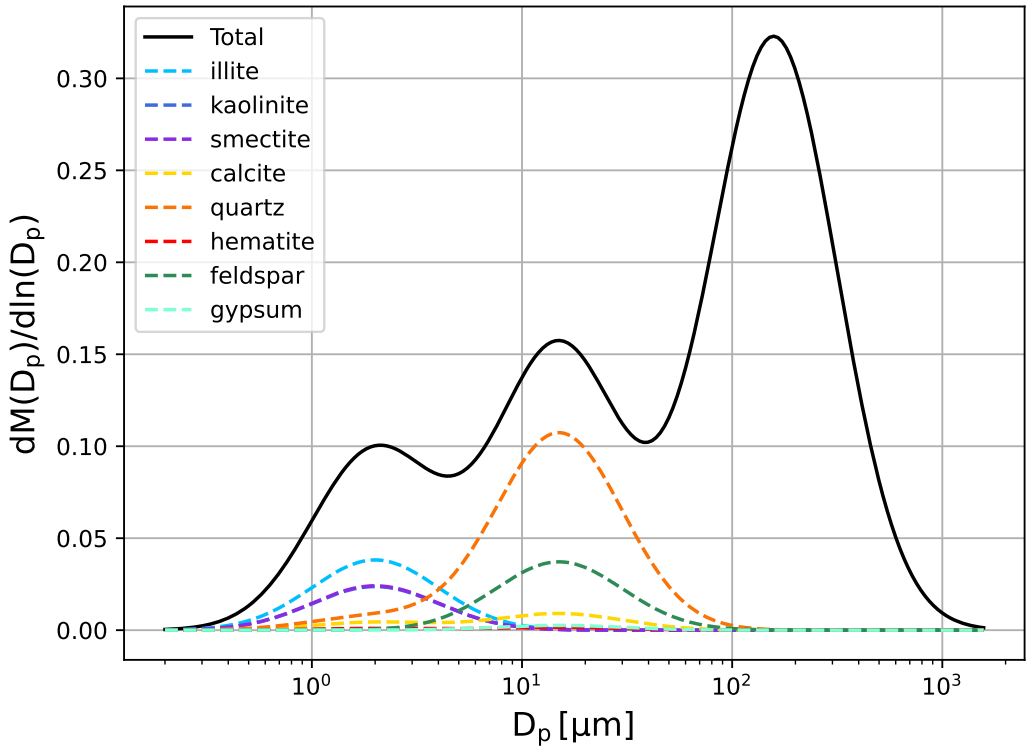

Figure 1. Mass size distribution of soil particles in a random grid cell (22.45°N, 20.9°E) in the Saharan Desert. In black, solid line the total mass size distribution is shown, three modes can be observed for the different soil size classes clay, silt and sand. In dashed, colored lines, the mass size distributions per mineral as given in the GMINER database are shown. Figure from Gómez Maqueo Anaya, Sofía (2025)

particle diameter D_p, modulated by an exponential cutoff, as expressed in the following relation:

$$\frac{dN}{dlnD_p} \propto \frac{1}{D_p^2} exp\left[-\left(\frac{D_p}{D_c}\right)^3\right] \text{for} D_p > D_s, \tag{7}$$

where D_s represents the "indivisible" size, where particles below this scale are resistant to further fragmentation due to their inherent particle cohesion. According to Kok (2011), this indivisible size corresponds to the wet-sieved PSD observed in soil samples, as wet sieving disperses soil aggregates until further breakdown becomes mechanically limited (Perlwitz et al., 2015a). Incorporating this concept, the emitted number size distribution can be formalized as:

$$\frac{dN}{dlnD_p} = \frac{1}{c_N D_p^2} exp\left[-\left(\frac{D_p}{D_c}\right)^3\right] \int_0^{D_p} p(D_s) dD_s, \tag{8}$$

where c_N is a normalization factor, and $p(D_s)$ represents the probability density function of the indivisible soil particle diameters after wet sieving. This formulation captures the physical constraint that emitted particles of size D_p cannot be formed

https://doi.org/10.5194/egusphere-2026-23
Preprint. Discussion started: 15 January 2026
© Author(s) 2026. CC BY 4.0 License.

from indivisible components larger than D_s. The integral term thus reduces the number of small-sized emitted particles if the soil has a limited abundance of fine indivisible grains, while the exponential cutoff suppresses emissions at larger diameters.

The BFT posits that the emitted number concentration of small dust particles is largely independent of the undispersed soil size distribution, with the upper limit of aggregate diameters (D_c) estimated at 12 ± 1 µm (Kok, 2011). In this framework, the PSD of emitted aggregates is skewed toward larger diameters compared to wet-sieved soil, consistent with observations by Kandler et al. (2009) and Enete (2012), which indicate that saltation-driven fragmentation preserves a greater fraction of mass in the silt-size range than suggested by wet-sieved samples. Perlwitz et al. (2015a) further show that roughly 45% of the silt-sized emitted mass originates from indivisible particles that would be classified as clay-sized in wet-sieved soils. To reconcile this discrepancy, they proposed an empirical correction that reallocates a fraction of clay-sized minerals from wet-sieved soils to the silt fraction, particularly phyllosilicates such as illite, kaolinite, and smectite, which are categorized in GMINER exclusively in clay size classes but contribute to silt-sized emissions in reality.

This adjustment is quantified using Equation (8) to derive a generalized ratio of emitted clay- to silt-sized particles, assumed to be spatially invariant and independent of local soil conditions. This simplifying assumption has been adopted in several modeling studies (Albani et al., 2014; Perlwitz et al., 2015a, b; Scanza et al., 2015; Pérez García-Pando et al., 2016; Gonçalves Ageitos et al., 2023). However, it applies only to particles below 20 µm, as larger particles are more sensitive to site-specific emission factors such as wind speed, soil properties, and surface roughness. Since GMINER defines the silt class up to 50 µm, a further adjustment is needed for particles in the 20–50 µm range. Perlwitz et al. (2015a) addressed this by scaling the clay contribution using measurements from Kandler et al. (2009), which provided empirical data on the coarse-mode mineral distribution of freshly emitted dust. Using Equation (8), they estimated a clay-to-silt ratio of 0.05 for diameters below 20 µm, which was reduced to 1.3% of the total emitted mass for the 0–50 µm range after volume-normalization for the coarser fraction.

This methodology rests on two critical assumptions. First, it assumes that the PSD measured at Tinfou by Kandler et al. (2009) is representative of other dust source regions. While this may not hold universally, the observed increase in silt fraction with particle diameter is consistent with the physical principle that the threshold friction velocity for emission decreases with particle size (Marticorena and Bergametti, 1995; Iversen and White, 1982). The approach also assumes that the emitted PSD is primarily determined by mineral-specific fragmentation, neglecting wind speed variations. This assumption is reasonable for particles below 20 µm, where Eq. (8) offers a reliable approximation, but becomes less reliable for coarser particles where emission dynamics are more sensitive to environmental conditions. Second, the model neglects modifications to the PSD caused by gravitational settling during transport to the Tinfou observation site. This simplification is justified by focusing only on measurements taken during high-concentration dust events, which are presumed to reflect recently emitted aerosols with minimal transport-induced size sorting.

This methodology is implemented here as the 'modified' approach, in which the dispersed soil size distribution from the GMINER SMA is adjusted to more realistically represent the aerosol size distribution observed in atmospheric dust. The formulation follows Perlwitz et al. (2015a), based on BFT. From GMINER, the mass fraction of each mineral $k \in \mathcal{M}$ in the clay (0-2 µm) and silt (2-50 µm) size categories is denoted by $m_k^c(s_t)$ and $m_k^s(s_t)$, respectively, where s_t is the arid soil type

https://doi.org/10.5194/egusphere-2026-23
Preprint. Discussion started: 15 January 2026
© Author(s) 2026. CC BY 4.0 License.

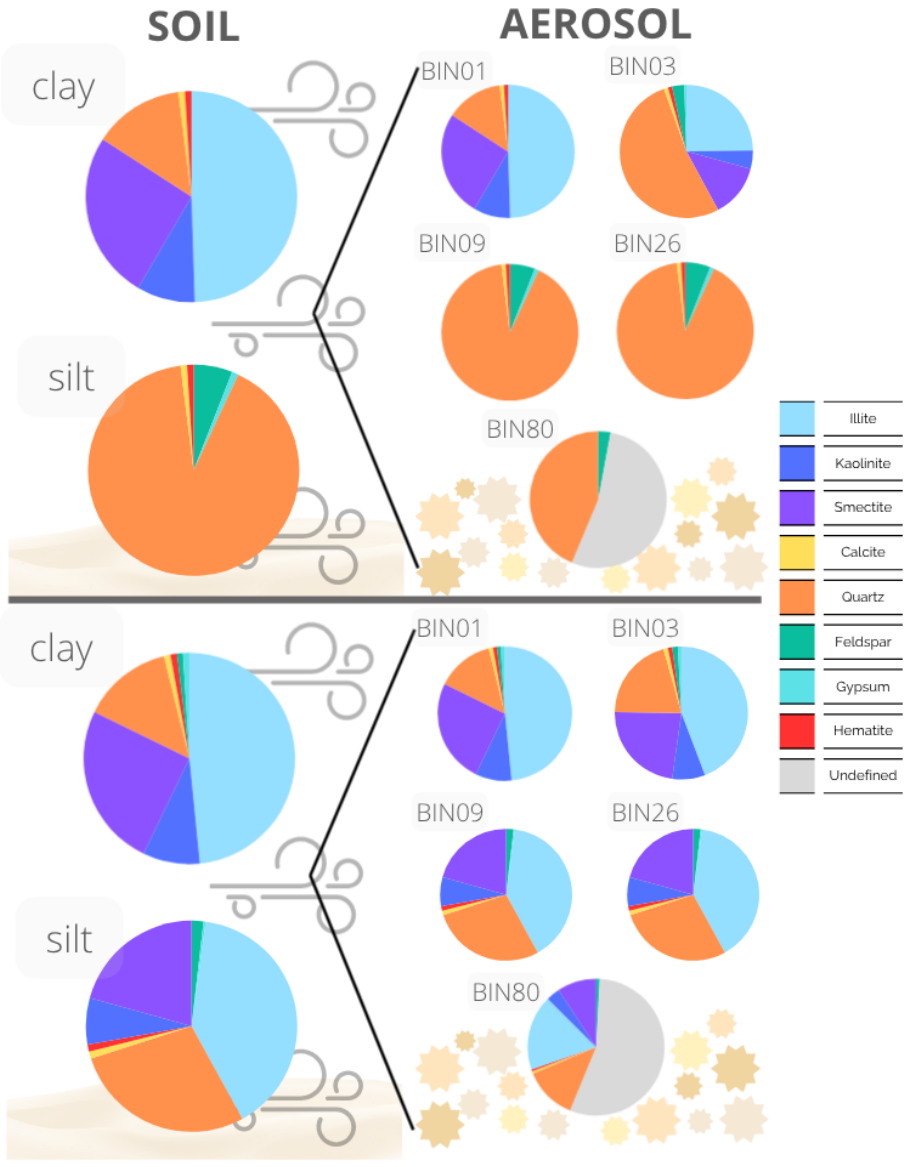

Figure 2. Larger pie charts represents mineral fraction soil distribution, clay represents particles with diameters below 2.5 µm and silt represents particles above. Smaller pie charts represent the mineral fractions of aerosols per size bin as classified in MUSCAT (Table 1). Upper panel shows the original mineral soil particle size distribution as obtained by GMINER and the subsequent mineral fractions in the aerosol bins mimicking that distribution. Lower panel shows the modifications to that mineral soil particle size distribution by following the modifications suggested by Perlwitz et al. (2015a), and Gonçalves Ageitos et al. (2023).

https://doi.org/10.5194/egusphere-2026-23
Preprint. Discussion started: 15 January 2026
© Author(s) 2026. CC BY 4.0 License.

provided by FAO74. These fractions are normalized for each soil type such that:

$$\sum_{k\in\mathcal{M}} m_k^{\mathrm{c}}(s_{\mathrm{t}}) = 1 \text{ and } \sum_{k\in\mathcal{M}} m_k^{\mathrm{s}}(s_{\mathrm{t}}) = 1, \tag{9}$$

with $|\mathcal{M}|$=8 minerals considered. To better reflect the emitted PSD, the BFT-based method distributes all minerals across both size categories, including those originally classified exclusively as clay- or silt-sized in GMINER.

To assign mineral fractions to the actual aerosol size categories, soil texture information from the SoilGrids database (Poggio et al., 2021) is incorporated. Let $m^{\mathrm{c}}(s_{\mathrm{x}})$ and $m^{\mathrm{s}}(s_{\mathrm{x}})$ denote the soil mass fractions of clay- and silt-sized particles, normalized such that:

$$m^{\mathrm{c}}(s_{\mathrm{x}}) + m^{\mathrm{s}}(s_{\mathrm{x}}) = 1. \tag{10}$$

The combined mineral mass fraction in each size category at each location is then computed by weighting the GMINER mineral fractions by the local soil texture proportions:

$$m_k^{\mathrm{c}}(s_{\mathrm{t}}, s_{\mathrm{x}}) = m^{\mathrm{c}}(s_{\mathrm{x}}) m_k^{\mathrm{c}}(s_{\mathrm{t}}), \quad m_k^{\mathrm{s}}(s_{\mathrm{t}}, s_{\mathrm{x}}) = m^{\mathrm{s}}(s_{\mathrm{x}}) m_k^{\mathrm{s}}(s_{\mathrm{t}}). \tag{11}$$

This ensures that the total mineral mass fraction across both size classes sums to unity:

$$\sum_{k\in\mathcal{M}} \left(m_k^{\mathrm{c}}(s_{\mathrm{t}}, s_{\mathrm{x}}) + m_k^{\mathrm{s}}(s_{\mathrm{t}}, s_{\mathrm{x}})\right) = 1. \tag{12}$$

In this formulation, mineral mass fractions vary spatially according to two factors: the arid soil type (s_{t}), which governs mineralogical composition, and the soil texture class (s_{x}), which determines the relative abundance of clay- and silt-sized particles.

Once the soil mineral fractions are obtained from Eq. (11), the next step is to derive the emitted mass fraction of each mineral in the clay and silt size categories. Denote by ϕ^{c} and ϕ^{s} the total emitted mass fractions of clay- and silt-sized aerosols, constrained by:

$$\phi^{\mathrm{c}} + \phi^{\mathrm{s}} = 1. \tag{13}$$

These totals are composed of contributions from all minerals $k \in \mathcal{M}$. Let $\phi_{\mathrm{k}}^{\mathrm{c}}$ and $\phi_{\mathrm{k}}^{\mathrm{s}}$ represent the emitted clay- and silt-sized fractions attributable to mineral k. They satisfy:

$$\phi^{\mathrm{c}} = \sum_{k\in\mathcal{M}} \phi_k^{\mathrm{c}} \text{ and } \phi^{\mathrm{s}} = \sum_{k\in\mathcal{M}} \phi_k^{\mathrm{s}}, \tag{14}$$

and consequently:

$$\sum_{k\in\mathcal{M}} (\phi_k^{\mathrm{c}} + \phi_k^{\mathrm{s}}) = 1. \tag{15}$$

Thus, the emitted mineral mass fractions across all species and size classes sum to unity. Following the BFT-based formulation, the global clay-sized emission fraction is prescribed as ϕ^{c}=0.013, constant across all locations. The contribution of

https://doi.org/10.5194/egusphere-2026-23
Preprint. Discussion started: 15 January 2026
© Author(s) 2026. CC BY 4.0 License.

mineral k to clay-size emissions is therefore given by:

$$\phi_k^{\mathrm{c}}(s_{\mathrm{t}}) = \phi^{\mathrm{c}} m_k^{\mathrm{c}}(s_{\mathrm{t}}), \quad \phi^{\mathrm{c}} = 0.013, \tag{16}$$

meaning that the proportion of emitted clay-sized dust mirrors the clay mineral fractions of the fully dispersed soil.

With ϕ^{c} prescribed, the total silt-sized fraction follows implicitly as:

$$\phi^{\mathrm{s}} = 1 - \phi^{\mathrm{c}} = 0.987. \tag{17}$$

For each mineral, the emitted silt-sized fraction $\phi_{\mathrm{k}}^{\mathrm{s}}$ has two sources: (1) particles originally present in the silt-size range, and (2) fragments of clay-sized particles that are mobilized through the disaggregation of aggregates during saltation. The latter is approximated by an empirical reallocation of clay mass into the silt fraction. This is expressed as:

$$\phi_k^{\mathrm{s}} = \vartheta\left(\gamma_k m_k^{\mathrm{c}}(s_{\mathrm{t}}, s_{\mathrm{x}}) + m_k^{\mathrm{s}}(s_{\mathrm{t}}, s_{\mathrm{x}})\right). \tag{18}$$

where γ_{k} is a mineral-specific reaggregation coefficient quantifying the clay-to-silt transfer, and ϑ is a normalization constant ensuring that the sum of all $\phi_{\mathrm{k}}^{\mathrm{s}}$ equals ϕ^{s}.

For simplicity, γ_{k} is assumed constant across minerals, with the exception of feldspar, gypsum, and quartz. Feldspar is typically overrepresented in the silt fraction due to its fragmentation behavior, while gypsum is soluble and exhibits distinct disaggregation and spatial patterns (Perlwitz et al., 2015a). Quartz, which dominates the coarse end of the size spectrum and shows little evidence of disaggregation, is prescribed with γ_{quartz}=0. Based on Eqs. (11) and (18), the emitted silt-sized fraction of mineral k is therefore expressed as:

$$\phi_k^{\mathrm{s}}(s_{\mathrm{t}}, s_{\mathrm{x}}) = \vartheta(s_{\mathrm{t}}, s_{\mathrm{x}}) \left[\gamma_k m^{\mathrm{c}}(s_{\mathrm{x}}) m_k^{\mathrm{c}}(s_{\mathrm{t}}) + m^{\mathrm{s}}(s_{\mathrm{x}}) m_k^{\mathrm{s}}(s_{\mathrm{t}})\right]. \tag{19}$$

In this formulation, γ_{k} acts to suppress the silt-size emissions of minerals such as quartz, while extending the contribution of clay-rich species (e.g., phyllosilicates) into the silt range. This redistribution reflects the contrasting aggregation behaviors of different minerals: quartz remains largely intact during saltation, whereas clay-dominated aggregates disintegrate, contributing to larger size classes.

Feldspar and gypsum require special treatment since they are present in both clay and silt fractions of atmospheric aerosols (e.g., Enete, 2012) but are absent from the clay fraction in the GMINER SMA. Consequently, Eq. (16) cannot be applied directly. Instead, their clay-size fractions are estimated following the approach of Gonçalves Ageitos et al. (2023), which uses proxy minerals and scaling ratios: for feldspar, the extension into the clay fraction is scaled according to the quartz clay-to-silt ratio:

$$m_{\mathrm{feldspar}}^{\mathrm{c}}(s_{\mathrm{t}}) = m_{\mathrm{feldspar}}^{\mathrm{s}}(s_{\mathrm{t}}) * \frac{m_{\mathrm{quartz}}^{\mathrm{c}}(s_{\mathrm{t}})}{m_{\mathrm{quartz}}^{\mathrm{s}}(s_{\mathrm{t}})}, \tag{20}$$

and for gypsum, the calcite clay-to-silt ratio is used:

$$m_{\mathrm{gypsum}}^{\mathrm{c}}(s_{\mathrm{t}}) = m_{\mathrm{gypsum}}^{\mathrm{s}}(s_{\mathrm{t}}) * \frac{m_{\mathrm{calcite}}^{\mathrm{c}}(s_{\mathrm{t}})}{m_{\mathrm{calcite}}^{\mathrm{s}}(s_{\mathrm{t}})}. \tag{21}$$

https://doi.org/10.5194/egusphere-2026-23
Preprint. Discussion started: 15 January 2026
© Author(s) 2026. CC BY 4.0 License.

To conserve the total clay-size mass balance (Eq. 9), the phyllosilicate fractions in the clay category are proportionally reduced by soil type.

A schematic representation of the 'modified' approach is shown in the lower panel of Fig. 2. In this framework, a substantial reduction of the quartz fraction is introduced, along with a redistribution of minerals across size classes. Specifically, phyllosilicates are incorporated into the silt fraction, while feldspar and gypsum are extended into the clay fraction. The application of Eqs. (19)–(21) thereby entails a relative decrease of feldspar and gypsum within the silt-size range, resulting from the additional contribution of phyllosilicates.

After constructing the adjusted mineral soil PSD, which better represents the composition of mineral aerosols at larger sizes, it is incorporated into the COSMO5.05-MUSCAT emission scheme. The underlying emission algorithm remains unchanged from the implementation described by Gómez Maqueo Anaya et al. (2024): the vertical emission flux in each MUSCAT size bin is scaled by the corresponding soil mineral fraction, with each mineral assigned to its own bin within the respective size category (see Table 1). In the revised configuration, the mineralogical SMA is updated to reflect the modified PSD, and additional bins are introduced to represent minerals that now occur simultaneously in both clay and silt size ranges.

4 In-situ dust sampling: dataset compilation and model comparison framework

4.1 Compilation of North Africa mineralogical measurements

To assess the atmospheric relevance of the modeled modifications, we compared COSMO5.05-MUSCAT model outputs with in-situ mineralogical measurements, taking into account the pronounced seasonal variability that governs Saharan dust emissions and their transport pathways. Because these seasonal effects are closely linked to mesoscale weather patterns and source activation, only measurements representative of NH winter months were retained to match the DUSTRISK 2022 campaign period (January–February 2022) (Gómez Maqueo Anaya et al., 2024) for this compilation.

The compilation builds on the dataset of Perlwitz et al. (2015b), augmented with additional North African measurements. The workflow for the selection of the measurements datasets is visualized in Figure 3. Long-term campaigns, here defined as sampling more than two dust events, were included only if their sampling period extended beyond NH summer months. The dataset was further expanded relative to the initial COSMO5.05-MUSCAT comparison with in-situ measurements (Fig. 5 in Gómez Maqueo Anaya et al. (2024)), and can be accessed through the zenodo repository . For long-term campaigns, we computed average mineral mass fractions over the DUSTRISK 2022 campaign simulation period and compared these against measurements. This approach was applied to the datasets of Adedokun et al. (1989); Enete (2012); Formenti et al. (2008); Kandler et al. (2009, 2011); Møberg et al. (1991) and Panta et al. (2023).

For shorter measurement campaigns covering up to two dust events, we employed a more detailed matching procedure (see the decision tree workflow from the "dust event analysis" box in Fig. 3). This approach combined two complementary datasets: (i) HYSPLIT back trajectories (Stein et al., 2015) and (ii) dust emission records from the MSG-SEVIRI Dust RGB product (EUMETSAT). Following the methodology of Schepanski et al. (2007), recently applied in Souza et al. (2025), we identified probable dust source regions by integrating these datasets. Simulated dust plumes were then selected to match the observed

https://doi.org/10.5194/egusphere-2026-23
Preprint. Discussion started: 15 January 2026
© Author(s) 2026. CC BY 4.0 License.

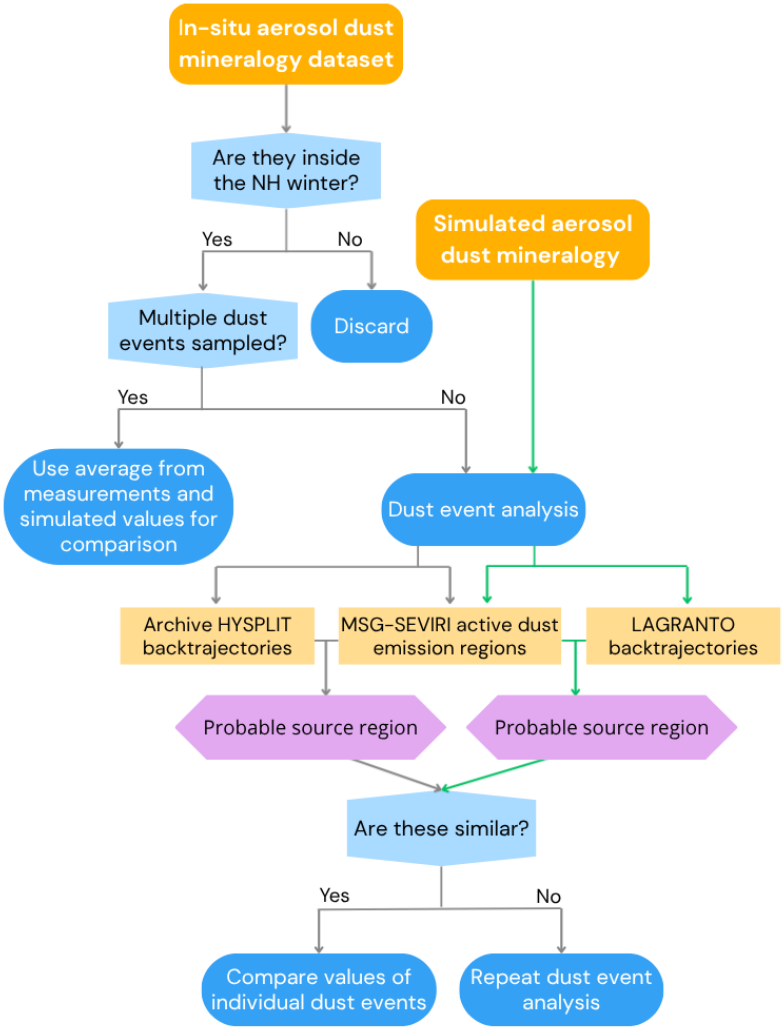

Figure 3. Schematic representation of the workflow used to select and compare in-situ mineral dust measurements with COSMO5.05-MUSCAT simulations. Primary datasets are displayed in yellow boxes with slanted corners and bold text. The analysis pathway for simulated mineralogy is depicted by green lines and arrows, while the in-situ measurement selection process is indicated by gray lines and arrows. Decision points are represented by blue hexagons, procedural steps by blue octagons, supplementary datasets by yellow rectangular boxes, and final outcomes by lavender octagons.

https://doi.org/10.5194/egusphere-2026-23
Preprint. Discussion started: 15 January 2026
© Author(s) 2026. CC BY 4.0 License.

transport pathways. Backward trajectories for simulated dust events were computed using the LAGRANTO tool (Miltenberger et al., 2013) driven by COSMO5.05 meteorological fields. Comparison with measurements only proceeded when similar dust source regions were identified through these datasets, allowing direct matching of individual dust plume measurements with model outputs.

Three campaigns required this detailed matching procedure: Alastuey et al. (2005), Jeong and Achterberg (2014), and Kandler et al. (2007). For the Alastuey et al. (2005) study, MSG-SEVIRI data were unavailable before 2004, so we used Meteosat-7 natural color imagery to identify a dust plume traveling from mid-southern Algeria to Tenerife on 29 July 2002. For the other two campaigns, observed plumes were individually matched to simulated events from corresponding source regions by combining HYSPLIT back trajectories (intersected with active MSG-SEVIRI dust emissions) with LAGRANTO back trajectories (intersected with the same emission areas). Several older measurements used by Perlwitz et al. (2015b), dating back to the 1970s, could not be reliably traced using this combined approach, and were therefore not compared with COSMO5.05-MUSCAT DUSTRISK outputs.

Although the selection criteria were applied rigorously, some historical dust plumes may not have been accurately matched to those simulated by COSMO5.05-MUSCAT. Deviations from typical seasonal transport patterns cannot be ruled out, as meteorological anomalies could have produced unusually strong emissions from certain source regions during the measurement periods. Such events may not be captured in the model output, which represent only January–February 2022, while the observations span a broader range of meteorological conditions. Furthermore, several measurement sites are located near major dust sources, where local emissions can dominate the observed mineral composition in ways that may not be fully resolved at the model's spatial resolution, as seen in the campaigns reported by Formenti et al. (2008); Kandler et al. (2009); Møberg et al. (1991) and Panta et al. (2023).

Additional uncertainty arises from inconsistencies in particle size classification across the measurement datasets. Some studies report only "bulk" mineral composition without specifying the particle size range; in these cases, the full COSMO5.05-MUSCAT size range (0.2–80 µm) was used for comparison. Other measurements adopt 'clay' and 'silt' categories, which are generally better defined but vary in the clay–silt boundary, reported between <2 µm and 2.5 µm (i.e., Kandler et al., 2009; Møberg et al., 1991). For these, model bins were mapped accordingly, with clay represented by BIN01 + 0.5 BIN03 and silt by 0.5 BIN03 + BIN09 + BIN26 + BIN80. When specific diameter ranges were reported (i.e., Kandler et al., 2007, 2009; Panta et al., 2023), the model bins containing more than 50% of the stated range were selected, and the average mineral mass fractions of those bins were used for comparison. These classification inconsistencies underscore the need for high-resolution, well-characterized, and concurrent measurement datasets. Such datasets were obtained during both the DUSTRISK and JATAC 2022 campaigns.

4.2 DUSTRISK 2022 campaign elemental composition

The DUSTRISK 2022 campaign took place in the Cape Verde archipelago during January and February 2022. Particulate matter sampling was conducted at two sites (named inflow and outflow) on the Cape Verde island of Santiago, where the inflow site is positioned upwind of urban areas and exposed mainly to continental air masses from Africa, in contrast to the

https://doi.org/10.5194/egusphere-2026-23
Preprint. Discussion started: 15 January 2026
© Author(s) 2026. CC BY 4.0 License.

Table 2. Mass percentage of key elements found in the COSMO5.05-MUSCAT simulated minerals. The smectite group is represented by the end-member montmorillonite, and feldspar is represented by a 1:1 average of microcline (K-feldspar) and albite (Na-feldspar). This selection is based on common mineralogical assemblages observed in Saharan dust aerosols (Scheuvens et al., 2013; Formenti et al., 2011, 2014).

Mineral	**Fe** (%)	**Si** (%)	**Al** (%)	**Mg** (%)	**K** (%)	**Ca** (%)	**S** (%)
Hematite	69.94	-	-	-	-	-	-
Illite	1.43	25.25	9.01	1.87	6.03	-	-
Kaolinite	-	21.76	20.90	-	-	-	-
Smectite	-	20.46	9.83	-	-	0.73	-
Quartz	-	46.80	-	-	-	-	-
Feldspar	-	30.89	10.23	-	14.05	0.76	-
Gypsum	-	-	-	-	-	23.28	18.62
Calcite	-	-	-	-	-	40.04	-

outflow site which is positioned outwind of the major urban area (Praia) (Bredeck et al., 2024; Souza et al., 2025). To ensure direct comparability with model simulations that represent only continental dust sources, the analysis presented here focuses exclusively on measurements from the inflow site. The inflow site in Santiago is located at 14°°59'24" N, 23°28'16" W, this site is characterized by strong prevailing northeast trade winds, with aerosol particles influenced by local marine emissions from the Atlantic Ocean and long-range transport of continental air masses from Africa, frequently carrying Saharan dust.

Particulate matter (PM) samples were collected during January and February 2022 using Digitel DHA-80 high-volume samplers (Walter Riemer Mess Technik, Germany) operating at an average flow rate of 500 L min^{-1}. At each site, separate PM2.5 and PM10 samplers were deployed. Sampling typically occurred over 24-hour periods (noon to noon); however, during pronounced dust events, sampling duration was shortened to capture peak concentrations. All samples were collected on Ahlstrom micro-quartz fiber filters (MK 360) (Bredeck et al., 2024; Souza et al., 2025).

Total reflection X-ray fluorescence (TXRF) spectroscopy was employed to determine elemental concentrations following the methodology previously described in detail (Fomba et al., 2020). Filter samples of 1.5 cm^2 area were prepared by digesting three 8 mm spots per filter in a HCl/HNO_3 mixture (0.375 mL and 1.125 mL, respectively) using a microwave digester (Mars 6, CEM, Germany). Internal standards (Sc/Co at 10 μL) were added to the digested solutions, which were then applied to siliconized quartz carriers, dried at 80°C, and analyzed using a Bruker S4 T-STAR instrument. This procedure determined concentrations of Al, Ti, Ca, K, Mg, S, Si, Cr, Mn, Fe, among other elements. Measurement precision was assessed by calculating relative errors from duplicate sample measurements.

Table 2 presents the mass percentages of selected elements within the simulated minerals. We focus on Fe, Si, Al, Mg, K, Ca, and S because these elements are commonly used for mineral identification in atmospheric dust studies (Kandler et al., 2018; Formenti et al., 2011, 2014; Panta et al., 2023; Rodríguez et al., 2020).

https://doi.org/10.5194/egusphere-2026-23
Preprint. Discussion started: 15 January 2026
© Author(s) 2026. CC BY 4.0 License.

The comparison between simulated and measured elemental compositions follows a three-step procedure: (1) Filter samples from inflow sites are identified, and measured elemental masses are normalized by total mass concentration to obtain elemental mass fractions. (2) Simulated mineral mass concentrations are extracted from the corresponding grid cells, temporally averaged over the filter sampling periods (±30-minute tolerance), and aggregated by size fraction. For PM2.5, we use MUSCAT's BIN01 + 0.5×BIN03; for PM10, we use BIN01 + BIN03 + BIN09 where available (e.g., the 'original' scheme defines phyllosilicates only through BIN03). (3) Mineral mass concentrations are converted to elemental mass concentrations by multiplying by their respective elemental mass percentages (Table 2), summing over minerals, and normalizing by total simulated mass concentration to yield elemental mass fractions.

In total reflection X-ray fluorescence (TXRF) analysis, the reproducibility of measurements on disk-shaped sample carriers is evaluated by performing multiple measurements on the same sample while rotating it. This approach helps account for any non-uniformity in the deposited residue. To assess measurement precision, each sample carrier was analyzed at 0° and 90° rotational positions, yielding replicate intensity data. The measurements used for validation were quality screened to ensure that measurements corresponding in their majority to mineral dust aerosols. Only samples with dust concentrations $\geq$38 µg/m^3 were included in the comparison (dust concentrations are derived following Souza et al. (2025) procedure). This screening resulted in 33 PM2.5 filters and 47 PM10 filters for the final validation dataset.

4.3 JATAC 2022 mineralogical composition

During the JATAC 2022 campaign, in-situ measurements of mineral dust aerosols were performed using Unmanned Aerial Vehicles (UAVs) over São Vicente, Cape Verde, throughout June 2022. The Cypurs Institute conducted 25 UAV flights, each equipped with Optical Particle Counters (OPCs) for fine- and coarse-mode height-resolved PSD observations. Dust particles were collected from the atmospheric layers using onboard impactor samples (Marinou et al., 2023), with a Giant Particle Collector (GPaC) capable of capturing particle diameters from nanometers up to tens of micrometers (Kezoudi et al., 2025, 2021). The GPaC's upper size limit depends on airspeed, pressure, and temperature; as a reference, during the SAMUM-2 campaign, particles up to 28.5 µm were successfully collected (Lieke et al., 2011).

Two OPCs were mounted on each UAV. The Universal Cloud and Aerosol Sounding System counted aerosols with diameters from 0.28 to 17.0 µm, while the Printed Optical Particle Spectrometer measured number concentrations in the 0.14–3 µm range (Kezoudi et al., 2021). OPC measurements were used to validate PSDs derived from collected dust samples, following the methodology of Panta et al. (2023).

Aerosol chemical composition and single-particle characteristics were analyzed using a scanning electron microscope coupled with Scanning Electron Microscope-Energy Dispersive X-ray spectrometry (SEM-EDX) to determine particle size, shape, and elemental composition. Back-scattered images were used to study particles with projected area diameters (PAD) >0.5 µm, where PAD ($D_\mathrm{p} = \sqrt{4A_\mathrm{p}/\pi}$, with A_p as the particle area) closely approximates aerodynamic diameter for dust (Aryasree et al., 2024; Kandler et al., 2018). SEM-EDX provides normalized atomic percentages for elements including: F, Na, Mg, Al, Si, P, S, Cl, K, Ca, Ti, V, Cr, Mn, Fe, Zn, and Pb. Major dust components are classified primarily based on the Al/Si ratio, with additional constraints from variations in Ca, Fe, Mg, K, and Na within aluminosilicates (Aryasree et al., 2024; Kandler et al.,

https://doi.org/10.5194/egusphere-2026-23
Preprint. Discussion started: 15 January 2026
© Author(s) 2026. CC BY 4.0 License.

2018, 2020; Panta et al., 2023). This method allows detection of particles up to 30 µm, with measurement precision for major compounds within 2% relative standard deviation (RSD), while minor compounds range from 10–20% for particles >3 µm, and can exceed to 100% for the smallest particles. Diameter measurement uncertainty decreases with size, from ∼1.5% RSD at 2 µm to <1% for particle diameters >3 µm (Kandler et al., 2018).

Certain minerals have well-defined compositions, such as gypsum, quartz, and calcite, making them readily identifiable through elemental ratios. Others, notably clay minerals like illite and smectite, exhibit substantial compositional variability, complicating their identification (Panta et al., 2023; Kandler et al., 2007, 2018; Rieder et al., 1998). Additionally, dust particles frequently occur as internal mixtures or aggregates rather than pure mineral phases. Consequently, the approach adopted here identifies the dominant mineral type within each particle. For single-particle quantification, an elemental index for element X is defined as the atomic fraction of that element relative to the sum of all quantified elements (Aryasree et al., 2024; Kandler et al., 2007, 2018; Panta et al., 2023):

$$mineral-like = \frac{X}{(Na+Mg+Al+Si+P+S+Cl+K+Ca+Ti+Cr+Mn+Fe)}. \quad (22)$$

Here, the element symbols represent the relative atomic percentage measured in each particle. Classification uses predefined rules based on the elemental index and additional ratios, determined by the dominance of specific elements or their combinations (e.g., Al, Si, Ca, Fe, Al/Si). Particle classes are named after their most prevalent chemical component(s), incorporating mineral phase terms where appropriate (e.g., gypsum, quartz), with labels assigned according to the best match to measured elemental concentrations.

Particles are grouped into mineralogical classes using rule sets derived from elemental ratios, taking into account ideal mineral compositions as well as natural variability and measurement uncertainty. While not all minerals strictly conform to the atomic ratios in Eq. (22), the classification focuses on minerals most relevant to the simulated compositions. Counting statistics for each particle group are used to estimate uncertainty by generating two-sided 95% confidence intervals under a binomial assumption. Table 3 provides detailed definitions of the mineral classes used in this study, the corresponding element X, and the criteria for *mineral-like* classification.

For iron oxide minerals such as hematite, the atomic ratio reported in Table 3 reflects the iron oxide content from a single-particle perspective. However, a significant fraction of iron in dust occurs within the crystal lattice of other minerals (Lafon et al., 2004; Zhang et al., 2015), necessitating an alternative approach to estimate total iron oxide content.

Following Aryasree et al. (2024), we use two parameters: (i) the total iron oxide percentage (Fe_{oxides}), which accounts for iron present either as pure oxy-hydroxides (e.g., hematite, goethite) or incorporated within mineral lattices, and (ii) the total Fe index, defined as the atomic ratio of Fe to the sum of all quantified elements, as in Eq. (22). The total iron oxide percentage is calculated as:

$$Fe_{\text{oxides}} = \left(\frac{m_{\text{Feox\%}}}{m_{\text{Fe\%}}}\right) * \left(\frac{M_{\text{Fe}}}{M_{\text{dry}}}\right) * 100, \quad (23)$$

where $m_{\text{Feox\%}}$ and $m_{\text{Fe\%}}$ are the mass fractions of iron oxides and elemental iron relative to the total dust mass, respectively, obtained from Table 3 in Di Biagio et al. (2019) for different Saharan source regions. M_{Fe} is the estimated Fe mass within a single particle from SEM-EDX measurements, and M_{dry} is the particle's dry mass.

https://doi.org/10.5194/egusphere-2026-23
Preprint. Discussion started: 15 January 2026
© Author(s) 2026. CC BY 4.0 License.

Table 3. Criteria for element-based identification of major minerals. Element symbols indicate atomic percent concentrations. When X corresponds to a single element or a sum of elements, it replaces X in Eq. (22). If X is not specified, the listed elemental ratio and its range are used directly to assign the mineral classification.

Class name	Atomic range	Value range
Quartz-like	X=Si	0.7 - 1.01
	Al/Si	0 - 0.22
	(Na+Mg+K+Ca+Al)/Si	0 - 0.2
	F/(F+Si)	0 - 0.499
Kaolinite-like	X=Al+Si	0.7 - 1.01
	Al/Si	0.5 - 1.5
	Fe/(Al+Si)	0 - 0.2
	Mg/(Al+Si)	0 - 0.2
	Ca/(Al+Si)	0 - 0.2
	Na/(Al+Si)	0 - 0.15
	K/(Si)	0 - 0.1
	(Na+Cl+2*S)/(Al+Si)	0 - 0.25
Illite-like	X=K+Al+Si	0.7 - 1.01
	Al/Si	0.45 - 1.5
	Fe/(Al+Si)	0 - 0.2
	Mg/(Al+Si)	0 - 0.2
	(Na+Ca)/(Al+Si)	0 - 0.2
	K/(Si)	0.1 - 1.01
	(Na+Cl+2*S)/(Al+Si)	0 - 0.25
Smectite-like	X=Mg+Al+Si	0.7 - 1.01
	Al/Si	0.5 - 1.5
	Fe/(Al+Si)	0 - 0.2
	Mg/(Al+Si)	0.2 - 1.01
	(Na+Ca)/(Al+Si)	0 - 0.2
	K/Si	0 - 0.1
	(Na+Cl+2*S)/(Al+Si)	0 - 0.25
Calcite-like	X=Ca	0.7 - 1.01
	X=Ca+Mg	0.7 - 1.01
	(Al+Si)/Ca	0 - 0.3
	Mg/Ca	0.3 - 3.0
	S/Ca	0 - 0.3
	Cl/Ca	0 - 0.19
	P/(Ca+P)	0 - 0.8
Gypsum-like	X=(Ca+S)	0.7 - 1.01
	Ca/(Ca+S)	0.2 - 0.8
	Mg/Ca	0 - 0.3
	Cl/Ca	0 - 0.3
Iron oxides-like	X=Fe	0.5 - 0.98999
	X=(F+Si)/F	0 - 0.499
	Cr/(Cr+Fe)	0 - 0.1
	Cl/(Cl+Fe)	0 - 0.1
	Ti/(Ti+Fe)	0 - 0.1
Feldspar-like	X=K+Al+Si	0.7 - 1.01
	X=Na+Al+Si	0.7 - 1.01
	X=Ca+Al+Si	0.7 - 1.01
	X=Na+Ca+Al+Si	0.7 - 1.01
	Al/Si	0.22 - 0.45
	(Na+K+Ca)/(Na+K+Ca+Al+Si)	0.15 - 0.25
	Fe/(Fe+Al+Si)	0 - 0.15

https://doi.org/10.5194/egusphere-2026-23
Preprint. Discussion started: 15 January 2026
© Author(s) 2026. CC BY 4.0 License.

Using Eq. (23), total iron oxide and hematite mass percentages are derived for each particle. For hematite specifically, the iron oxide mass fraction in Eq. (23) is replaced by the hematite mass fraction reported in Table 3 of Di Biagio et al. (2019).

The calculated mineral mass fractions are then compared against COSMO5.05-MUSCAT simulation outputs, where simulated mineral compositions are extracted from the corresponding grid cells and averaged over both the sampling periods and specified altitude ranges. In addition to the mineralogical composition comparison, elemental mass fractions are evaluated using the model validation methodology described in the previous section (Section 4.2). Filter measurements were quality screened to ensure sufficient particle counts for robust statistical analysis, where only filters containing 1000–2000 particles were included in the comparison. This screening resulted in measurements from 17 filters that were taken into account for the final validation dataset.

5 Model validation

5.1 Northern Africa

To assess the implementation of the 'modified' mineral simulation approach in the COSMO5.05-MUSCAT emission scheme (Section 3.2), first we compare the results with the MONARCH reference shown in Fig. 1 of Gonçalves Ageitos et al. (2023). The comparison is performed for the same soil type, Xerosols Haplic, located in the northwestern Sahara. Figures 4a) and A) show results obtained with the 'original' method based on the undisturbed mineralogical database PSD, whereas Figs. 4b) and B) depict the normalized PSD emission fluxes after modifying the mineralogical database.

The two models differ in how the mineral PSD changes are integrated into the emission calculation. MONARCH modifies the mineral PSD directly within its emission parameterization, computing mineral emissions up to 20 µm using the updated BFT formulation of Kok (2011) (Section 3.2). In contrast, COSMO5.05-MUSCAT adjusts the mineral soil PSD during preprocessing, prior to emission flux calculation. The modified soil PSD is then combined with the Marticorena and Bergametti (1995) emission scheme and distributed across MUSCAT's vertical bin structure. MONARCH also applies a finer size discretization and a narrower size range than COSMO5.05-MUSCAT: it uses eight bins extending to 20 µm, while COSMO5.05-MUSCAT employs five broader bins reaching 80 µm (Table 1). Despite these structural differences, both models show clay fractions largely unchanged and a consistent redistribution pattern, with phyllosilicates shifted toward silt-sized categories and a proportional reduction of quartz, as expected.

Nevertheless, notable differences appear. In the MONARCH reference, quartz fractions increase progressively with particle sizes above 2 µm, while COSMO5.05-MUSCAT shows only a slight rise between the third and fourth bins, with no further increase toward larger sizes. As a consequence, MONARCH exhibits a continuous decrease of phyllosilicates in the larger bins, a feature absent from the COSMO5.05-MUSCAT modified PSD. These discrepancies reflect the coarser bin resolution and broader size range of COSMO5.05-MUSCAT, as well as differences in how the emission schemes interact with the SMA.

To evaluate whether the 'modified' approach improves the representation of dust mineral aerosol composition, a simulation for the DUSTRISK 2022 campaign was conducted using the approach, shown in yellow solid stars in Fig. 5. A direct comparison is made with the 'original' approach. Mineral mass percentages are compared then between the North Africa compilation

https://doi.org/10.5194/egusphere-2026-23
Preprint. Discussion started: 15 January 2026
© Author(s) 2026. CC BY 4.0 License.

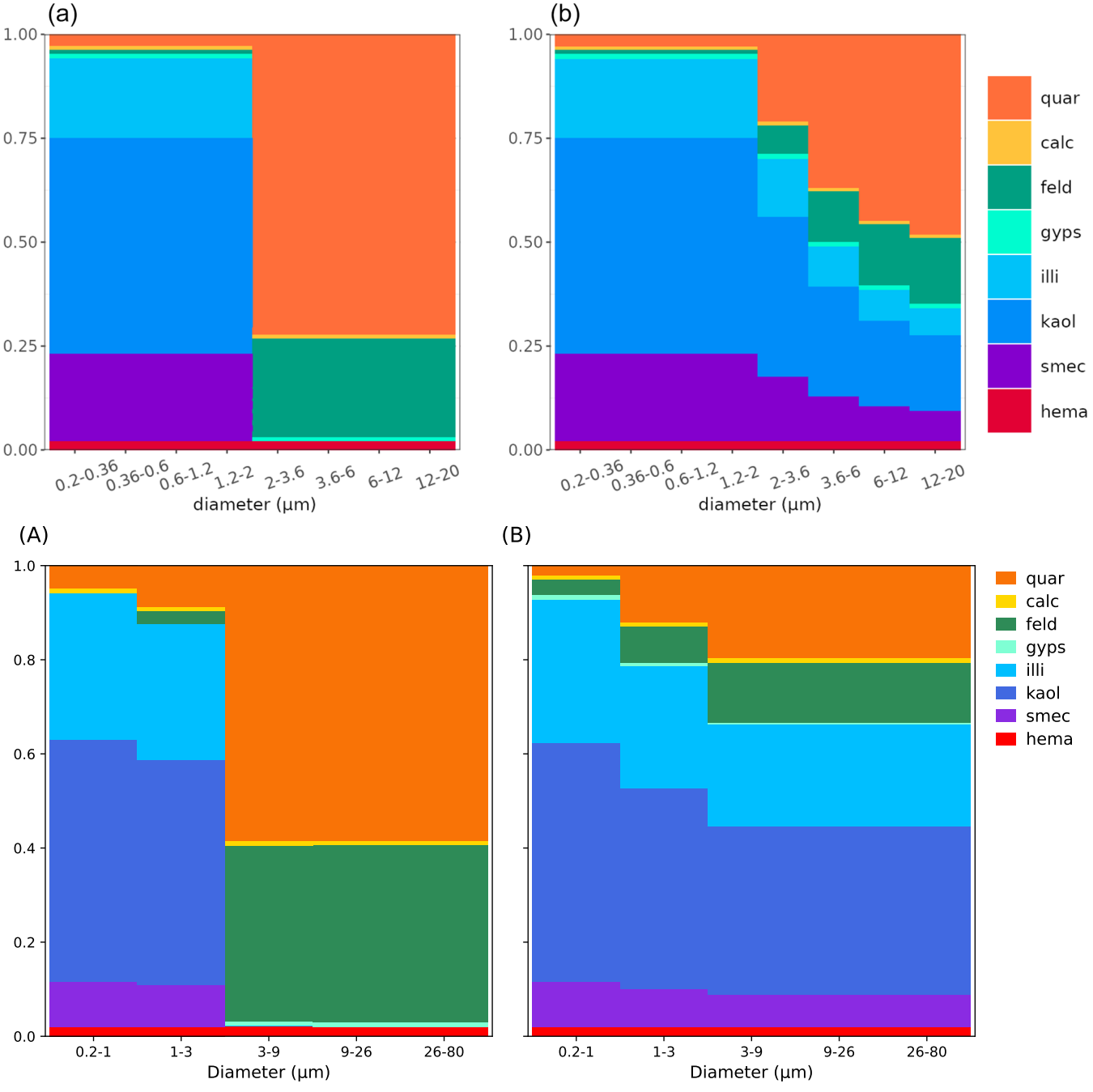

Figure 4. (a) & (A): soil mineral PSDs; (b) & (B): aerosol mineral PSDs. Upper panel: MONARCH results, copied from Gonçalves Ageitos et al. (2023); normalized mass size distribution of minerals for the Xerosols Haplic soil type according to Claquin et al. (1999)'s database. Lower panel: COSMO5.05-MUSCAT results; normalized mass size for the Xerosols Haplic soil type according to GMINER. (B) aerosol PSD is a result of modifying the mineralogical dataset by following a BFT-based approach (Perlwitz et al., 2015a; Gonçalves Ageitos et al., 2023). Quar: quartz; calc: calcite; feld: feldspars; gyps: gypsum; illi: illite; kaol: kaolinite; smec: smectite; hema: hematite.

https://doi.org/10.5194/egusphere-2026-23
Preprint. Discussion started: 15 January 2026
© Author(s) 2026. CC BY 4.0 License.

of measured values and the simulation approaches. The results are summarized in Fig. 5, with uncertainties indicated by error bars when reported.

The differences between the two simulations are consistent with expectations. Bulk measurements indicate an increase in phyllosilicates (illite and kaolinite in Fig. 5) under the 'modified' approach, accompanied by a decrease in quartz mass fractions. For the clay-only measurements, phyllosilicates are slightly reduced, most clearly reflected in the illite values exceeding 30% in Fig. 5. When averaged over the full simulation period, calcite content increases by 12%, hematite by 17%, and gypsum by 6% compared to the 'original' mineralogical scheme. The strongest changes occur for kaolinite and illite, which increase on average by 133% relative to their previous mass percentages, followed by smectite with a 128% increase. Conversely, quartz and feldspar fractions decrease substantially, by 53% and 49%, respectively.

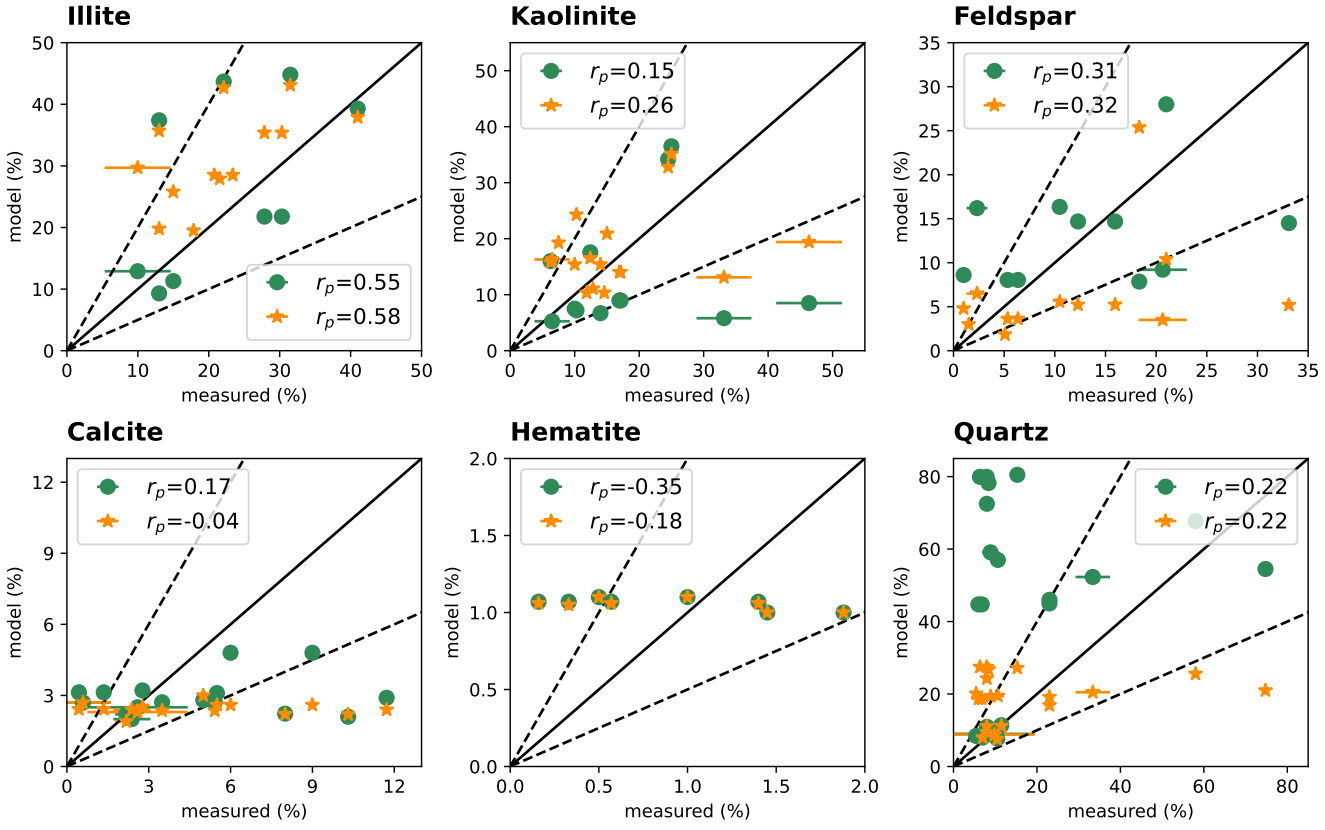

Figure 5. Modified from Fig. 5 in Gómez Maqueo Anaya et al. (2024). Scatterplots of mineral mass percentages of illite, kaolinite, feldspar, calcite, hematite and quartz measured vs. simulated by COSMO5.05-MUSCAT, the 'original' mineral emission scheme in green solid dots while the 'modified' version is shown in yellow solid stars. The dashed lines represent the ratios of 2:1 and 1:2 between the simulated and observed mineral percentages. The error bars are present when reported in the measurements. Pearson correlation coefficients are shown in the legend represented by r_p.

https://doi.org/10.5194/egusphere-2026-23
Preprint. Discussion started: 15 January 2026
© Author(s) 2026. CC BY 4.0 License.

Overall, kaolinite is the only mineral that shows a clear improvement in correlation with measurements when using the 'modified' approach, as indicated by the Pearson correlation coefficients (r_p) in Fig. 5. Illite also exhibits a marginal improvement based on the change in correlation coefficients. The broad definition of illite complicates its identification (Rieder et al., 1998, and references therein), contributing to this ambiguity. Importantly, some measurements that could not previously be compared due to size limitations are now accessible. On average, both kaolinite and illite are slightly overrepresented in the 'modified' simulation. For illite, the overestimation already present in the 'original' approach is further amplified, whereas kaolinite shifts from underestimation in the 'original' scheme to slight overestimation in the 'modified' one.

Feldspar shows little change in correlation between the two approaches, although its simulated mass fractions are substantially reduced in the 'modified' scheme. Both schemes underestimate feldspar compared to observations, but the 'modified' approach now enables additional comparisons by including feldspar in the lowest size bin (see Eq. 20). Quartz correlations likewise remain unchanged, but its content is strongly reduced. This reduction has a marked effect on the difference between model and measured percentages: the overestimation of quartz decreases from a residual average of ∼30% with the 'original' scheme to only 1% with the 'modified' scheme.

Calcite representation worsens, remaining underestimated in both schemes. Hematite correlations remain poor, with negative r_p values in both cases. The quantification of hematite is subject to large uncertainties, as it occurs both as individual particles and within the crystal lattice of other minerals (Lafon et al., 2004; Zhang et al., 2015). While the average hematite mass fraction increases by 17% across the simulation period (Sect. 3.2), this increase is not reflected in Fig. 5, where both mineralogical schemes yield similar values.

Potential biases in the measurement dataset should also be considered. For instance, the inclusion of the FRAGMENT campaign added ∼40% more data to the reference set (Fig. 5 in Gómez Maqueo Anaya et al. (2024)). These measurements, reported by Panta et al. (2023), were collected in the Drâa Valley, Morocco, near active dust source regions. Such localized influences may not be captured by the model, whose 28 km spatial resolution represents grid-cell averages and does not resolve small-scale convective events. Likewise, several other campaigns included in the comparison were conducted close to dust sources, reflecting local emissions rather than regional transport observations. As a result, the observations may not fully represent the broader mineral fraction distributions that the model is designed to simulate. Seasonal coverage also plays a role: while some campaigns spanned transitional months with shifts in dominant source regions, the simulations are restricted to NH winter (January–February), potentially missing these seasonal variations (Gebauer et al., 2025). Overall, the limited correlation improvements and the inability to draw definitive conclusions are driven by both the scale mismatch between point measurements and grid-cell averages, as well as the temporal and spatial representativeness of the observations, which introduce multiple sources of uncertainty.

5.2 Cape Verde - DUSTRISK 2022 campaign

The regional analysis presented above evaluated mineral composition across multiple measurement campaigns spanning different years and locations, where temporal matching between observations and simulations was based on seasonal patterns rather than exact timing. While informative for assessing broad model performance, this approach lacks the precision needed

https://doi.org/10.5194/egusphere-2026-23
Preprint. Discussion started: 15 January 2026
© Author(s) 2026. CC BY 4.0 License.

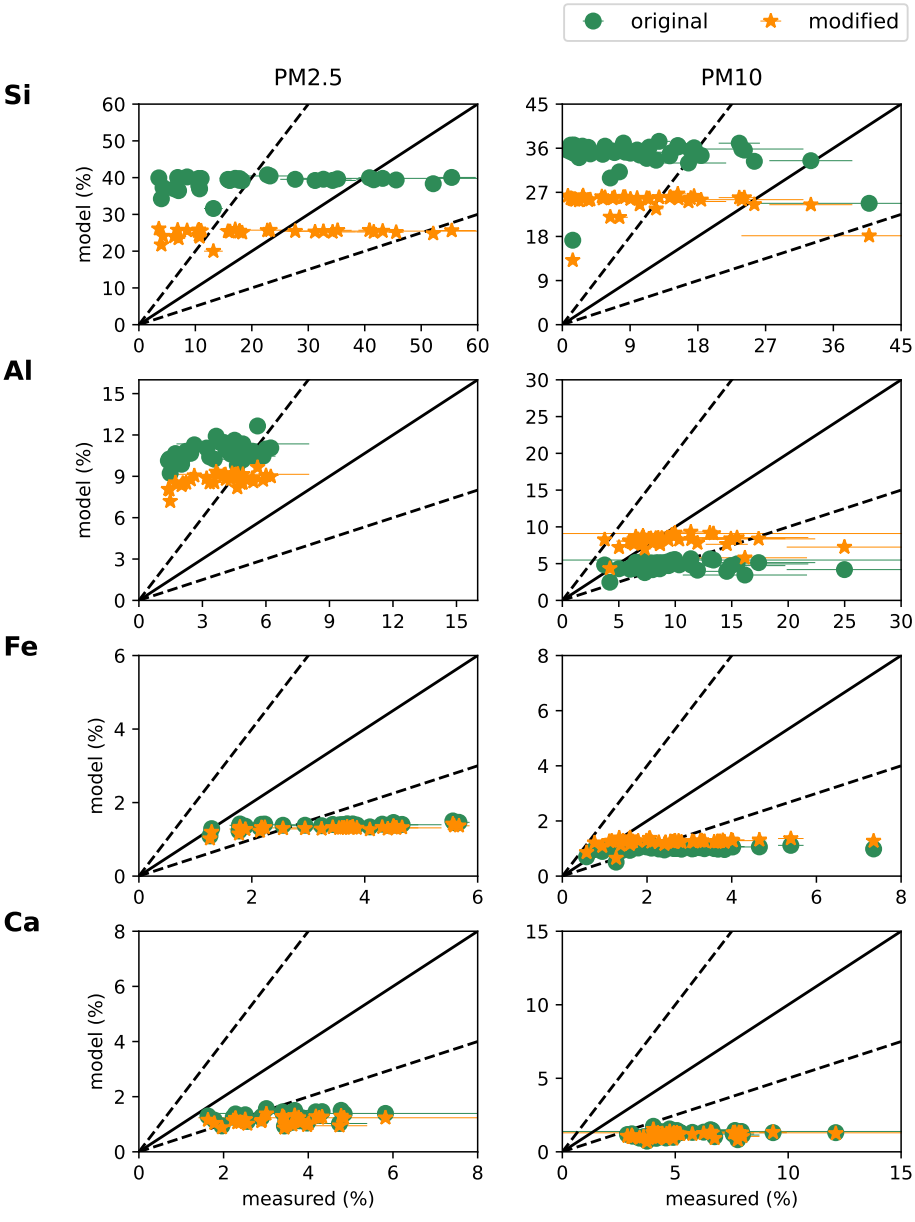

Figure 6. Scatterplots comparing observed elemental mass percentages of Si, Al, Fe, and Ca against simulated values from COSMO5.05-MUSCAT. Simulated values were derived by multiplying modeled mineral mass by their respective elemental compositions (detailed in Table 2). Green solid circles indicate the 'original' mineral emission scheme, while yellow solid stars represent the 'modified' version. Column headers denote size classifications based on in-situ filter measurements: PM2.5 and PM10. The error bars are represent the measurements' standard deviation. Dashed lines mark the 2:1 and 1:2 ratios between simulated and observed mineral percentages.

https://doi.org/10.5194/egusphere-2026-23
Preprint. Discussion started: 15 January 2026
© Author(s) 2026. CC BY 4.0 License.

for stringent validation. The DUSTRISK campaign (January–February 2022) addresses this limitation by providing high-resolution measurements of elemental composition and particle size distributions that coincide exactly with the simulation period. Cape Verde's role as a primary receptor site for Saharan dust transport makes these measurements particularly valuable for evaluating the 'modified' mineralogical scheme. Additionally, validating the model through elemental mass fractions calculated from simulated mineral compositions via Table 2 provides a complementary approach for validation of simulated mineralogical content.

The scatterplots in Fig. 6 demonstrate marked differences in performance between the 'original' and 'modified' mineral emission schemes when evaluated across elemental composition and particle size categories. The 'modified' approach shows improved representation of silicate content, largely attributable to decreased simulated quartz concentrations. In PM2.5, the overestimation by the model decreases from a mean residual of +18% to +4% when applying the 'modified' scheme, while in PM10, the overestimation is reduced as reflected in the change of average residuals from +25% to +15%. However, these Si comparisons must be interpreted cautiously due to potential contamination from the quartz-based filter material used for sampling.

Measured aluminum content shows pronounced size fractionation, with PM10 exhibiting both elevated concentrations and increased variability relative to PM2.5. For clay-sized particles (PM2.5), the modest reduction in phyllosilicate mass under the 'modified' scheme reduces model overestimation, with mean residuals improving from +7% to +5%. For the silt-size fraction (PM10), an increase in phyllosilicate concentrations likewise strengthens model performance, diminishing the underestimation from a residual mean of -5% to -1%.

Both emission schemes substantially underestimate iron content, with negligible improvement in the 'modified' version. This underestimation contrasts sharply with the mineral-level evaluation (Fig. 5), where hematite concentrations showed reasonable agreement with observations. Although Fe occurs in other simulated minerals, notably illite and certain smectite formulations, these secondary sources do not account for the simulated Fe under representation. This discrepancy between elemental Fe underestimation and adequate hematite simulation highlights a key feature of atmospheric iron. Fe, especially as iron oxides, occurs predominantly as coatings or inclusions on other mineral phases rather than as isolated hematite particles (e.g., Lafon et al., 2004; Kandler et al., 2007; Zhang et al., 2015). Such mineralogical complexity poses fundamental challenges for models that assume external mineral mixing, simulating each mineral as a single particle. Calcium shows comparable systematic underestimation in both schemes, but in this case, it mirrors the underrepresentation of calcite, the dominant Ca-bearing mineral in the model.

The potassium content shown in Figure 7 reveals an intriguing size-specific improvement under the 'modified' scheme. For PM2.5, the modified approach yields substantially better agreement with observations, reducing the model's overestimation from a mean residual of +2% to +1%, while PM10 shows negligible change between schemes. The reduction of bias for the clay sized particles stems primarily from the addition of the feldspar fractions to this size category. The improvement is particularly noteworthy given that the preceding mineral-specific feldspar comparison (Fig. 5) revealed neither substantial differences between schemes nor strong correlations with measurements. This discrepancy highlights the value of elemental-

https://doi.org/10.5194/egusphere-2026-23
Preprint. Discussion started: 15 January 2026
© Author(s) 2026. CC BY 4.0 License.

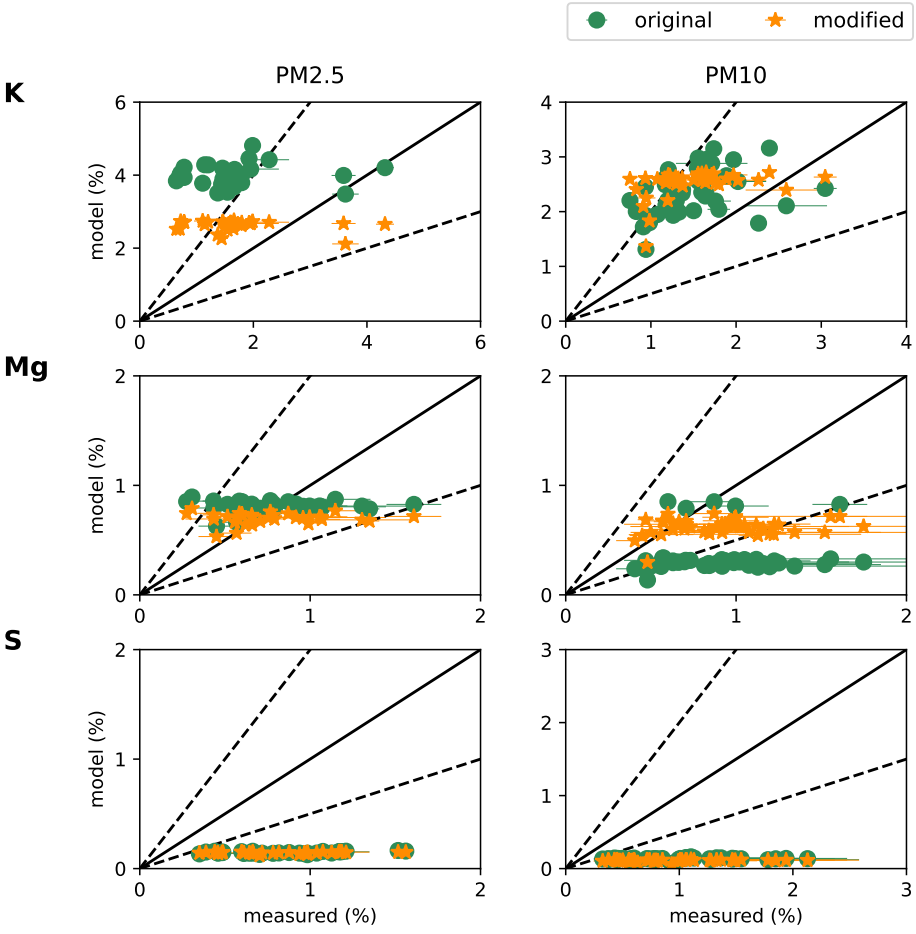

Figure 7. As in Fig. 6 but for K, Mg and S.

level validation in assessing modifications to mineralogical emission schemes, as changes that appear modest in mineral-specific comparisons may produce clearer signals when evaluated through their elemental signatures.

Magnesium displays a size-dependent pattern analogous to that observed for aluminum. Although the earlier illite comparison did not strongly suggested improvements by the 'modified' scheme, an enhancement on the representation emerges from the Mg elemental analysis. For PM2.5, the 'original' scheme's overestimation transitions to a slight underestimation under the 'modified' approach, with changes on the order of 0.05% in mean residuals. In PM10, the model's underestimation diminishes considerably, with mean residuals between simulated and measured values reduced by half.

Sulfur remains systematically and substantially underestimated by the model across both emission schemes, a deficiency directly attributable to the well-documented underrepresentation of gypsum content in SMAs (Gonçalves Ageitos et al., 2023; Song et al., 2024).

https://doi.org/10.5194/egusphere-2026-23
Preprint. Discussion started: 15 January 2026
© Author(s) 2026. CC BY 4.0 License.

The elemental comparisons reveal that while the 'modified' emission scheme successfully addresses several key biases on the mineralogical representation, particularly for Si, Al, and Mg, systematic underestimations persist for certain elements, notably Fe, Ca, and S. However, interpretation of these discrepancies must account for the likelihood that the measured aerosol samples contain contributions from non-mineral sources. The sampling campaign employed long integration periods during the NH winter season, a period characterized by intense biomass burning activity across the Sahel region (Tesche et al., 2011). Biomass burning emissions are known to contribute substantial quantities of K (Dang et al., 2022), which can confound interpretations of K derived from feldspars and clays in mineral dust (Formenti et al., 2011; Kandler et al., 2007). Additionally, biomass burning can produce fine-mode particles enriched in elements such as Al and Mg through the combustion of vegetation and soil dust entrained in fire plumes (Paris et al., 2010). Disentangling these source contributions would require either shorter sampling intervals, complementary measurements of biomass burning tracers (e.g., black carbon or levoglucosan), or selective sampling of the elevated Saharan Air Layer (SAL), which is more likely less contaminated by other aerosol types.

The JATAC 2022 campaign provides this latter advantage. Conducted during the NH summer when the SAL is characteristically elevated, JATAC measurements predominantly captured mineral dust with minimal biomass burning interference. This cleaner sampling environment enables a more direct evaluation of the model's mineral composition representation without the confounding factors present in the DUSTRISK NH winter measurements.

5.3 Cape Verde - JATAC 2022

5.3.1 Mineral comparison

The comparison between JATAC 2022 in-situ 'mineral-like' dust aerosol measurements and COSMO5.05-MUSCAT simulated minerals is presented in Fig. 8 for clay minerals, Fig. 9 for silt minerals, and Fig. 10 for hematite. Both the 'original' scheme (Gómez Maqueo Anaya et al., 2024) and the 'modified' scheme (Section 3.2) are evaluated. Measurements were binned according to COSMO5.05-MUSCAT size categories (BIN01, BIN03, BIN09, BIN26); BIN80 measurements are unavailable due to the 30 µm detection limit of SEM-EDX (Kandler et al., 2018).

For clay minerals (illite, kaolinite, and smectite in Fig. 8), the model generally overrepresents total phyllosilicates. A key improvement of the 'modified' scheme is the inclusion of clay minerals in coarser size bins, enabling direct comparison beyond the sub-2.5 µm fraction. In BIN01, both approaches show similar overrepresentation. In BIN03, the 'original' scheme underestimates phyllosilicates, while the 'modified' scheme overestimates them by an average of 17%.The best agreement is found in BIN09 with an average residual of +9%, though overestimation increases again in BIN26 (+15%). Looking at individual clays, measured illite and smectite fractions are extremely low, falling outside the compiled dataset shown in Fig. 5, leading to systematic overestimation in the model. This partly reflects known challenges in identifying these minerals in measurements (e.g., Rieder et al., 1998), which introduce uncertainties in both observations and mineralogical databases. Kaolinite shows the opposite behavior, with modeled values underestimates its content overall. The 'modified' scheme reduces the residual in BIN03 but maintains underrepresentation in larger bins.

https://doi.org/10.5194/egusphere-2026-23
Preprint. Discussion started: 15 January 2026
© Author(s) 2026. CC BY 4.0 License.

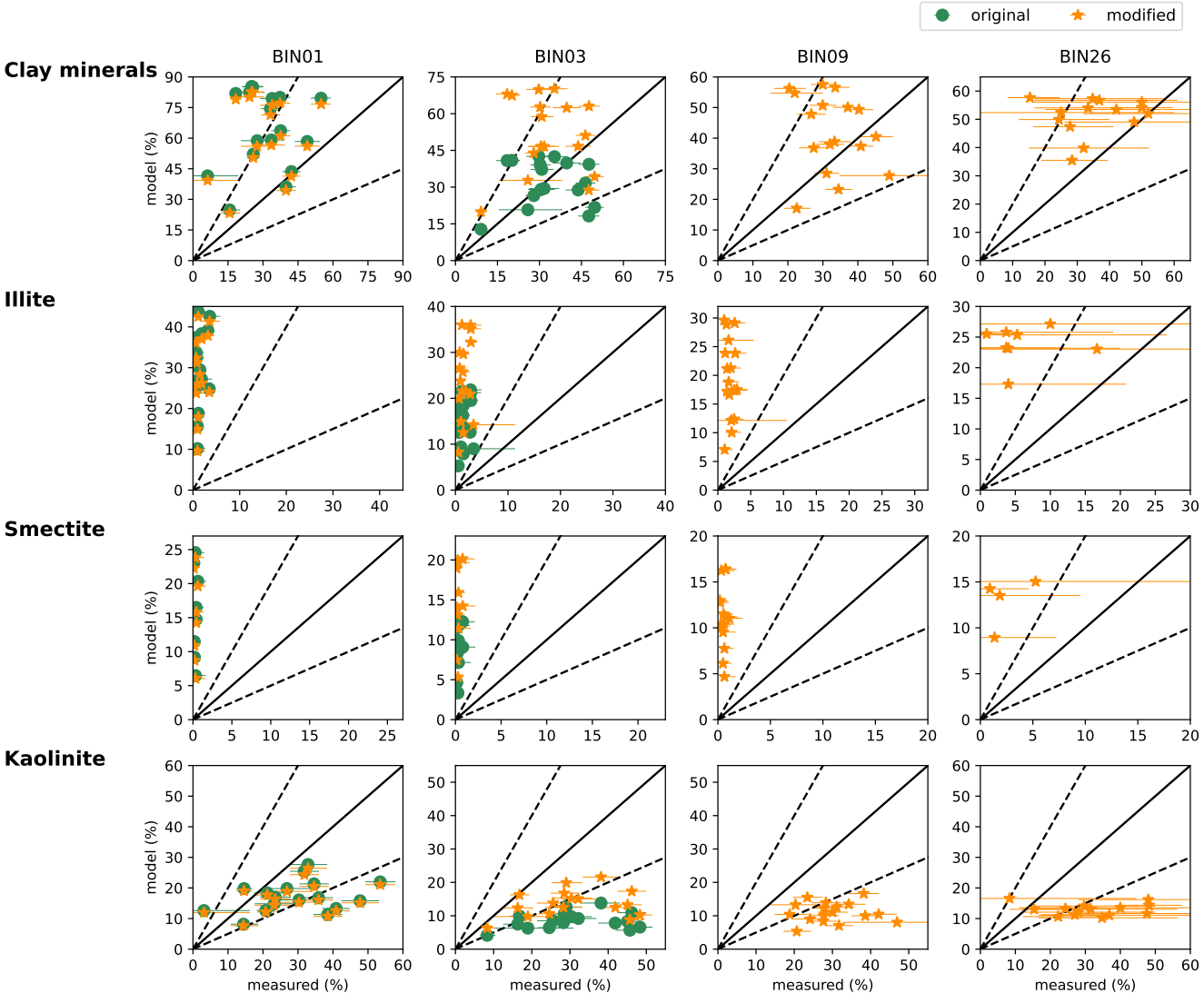

Figure 8. Scatterplots of minerals mass percentages of clay minerals, i.e., illite, smectite, and kaolinite, grouped and individually vs. simulated by COSMO5.05-MUSCAT. 'original' mineral emission scheme in green solid dots while the 'modified' version is shown in yellow solid stars. The titles of the columns are size classifications from COSMO5.05-MUSCAT, the diameter ranges they represent are described in Table 1. The dashed lines represent the ratios of 2:1 and 1:2 between the simulated and observed mineral percentages. The error bars represent the lower and upper limits of the confidence intervals (between 2.5% and 97.5%).

https://doi.org/10.5194/egusphere-2026-23
Preprint. Discussion started: 15 January 2026
© Author(s) 2026. CC BY 4.0 License.

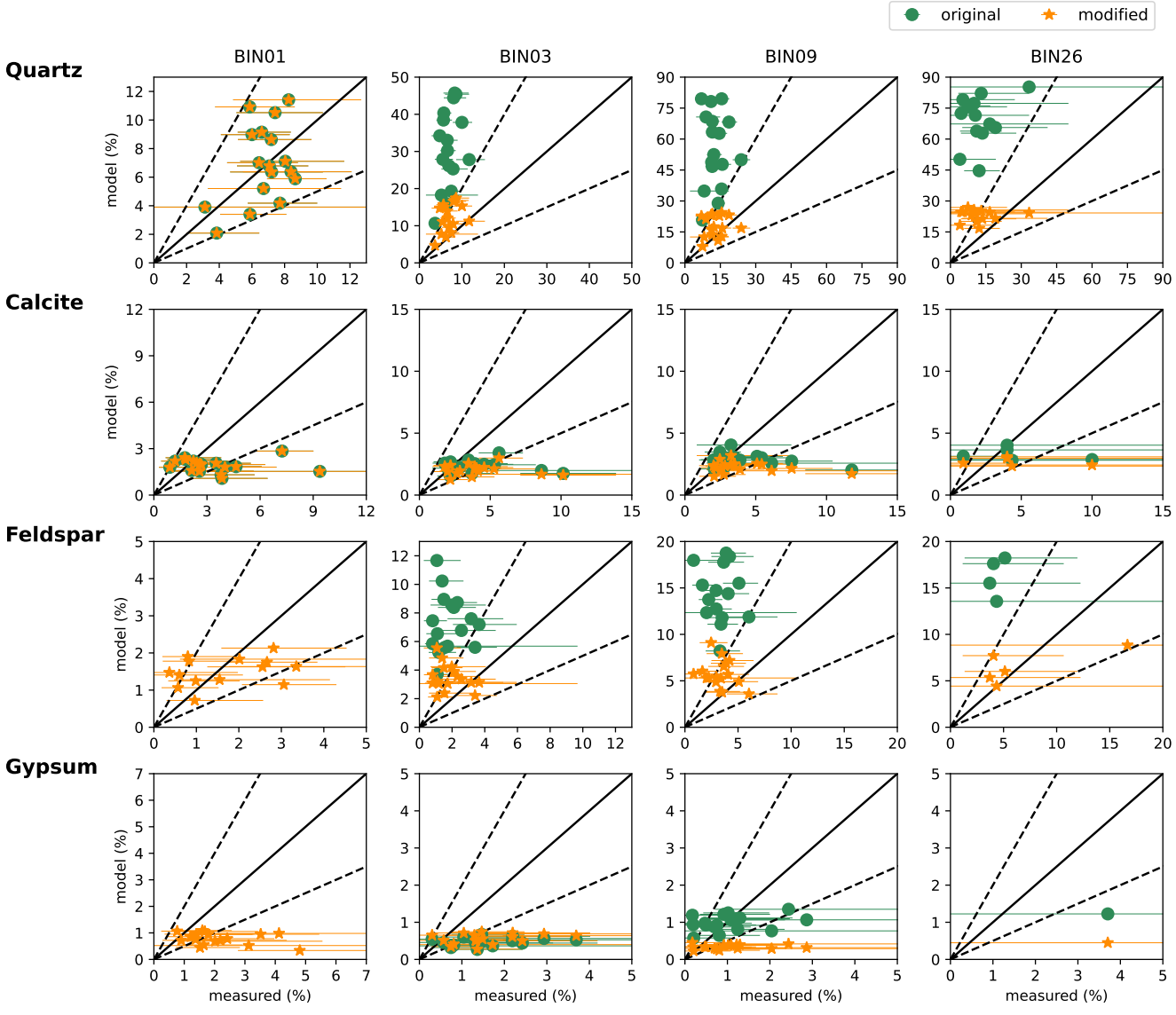

Figure 9. As in Fig. 8 but for silt minerals, i.e., quartz, calcite, feldspar, and gypsum.

https://doi.org/10.5194/egusphere-2026-23
Preprint. Discussion started: 15 January 2026
© Author(s) 2026. CC BY 4.0 License.

A related study by Gonçalves Ageitos et al. (2023) found that the GMINER SMA (Nickovic et al., 2012) generally outperforms Journet et al. (2014) SMA in reproducing the spatial distribution of phyllosilicates, although it tends to overestimate kaolinite and smectite while underestimating illite across the Sahara region. Their analysis also showed that, for fine clay-sized fractions, illite is often overestimated near dust sources but underestimated during long-range transport, whereas coarser silt-sized illite is typically underestimated. In contrast, our comparison with JATAC 2022 measurements shows consistent overestimation of illite across all size bins.

For silt-sized minerals (Fig. 9), the 'modified' scheme strongly reduces quartz overestimation. Average residuals decrease from +23%, +41%, and +60% in the 'original' scheme for BIN03, BIN09, and BIN26, respectively, to just +5–11%, while calcite remains underestimated across all bins with little improvement under the 'modified' scheme, consistent with earlier findings for 2–20 µm particles (Gonçalves Ageitos et al., 2023). Feldspar shifts from strong overestimation in the 'original' approach to nearly unbiased results in BIN03 and BIN09 (+1–2%) and slight underestimation in BIN01 and BIN26 (-∼0.5%). Gypsum is consistently underestimated in both schemes, with higher average residuals resulting from the implementation of the 'modified' scheme.

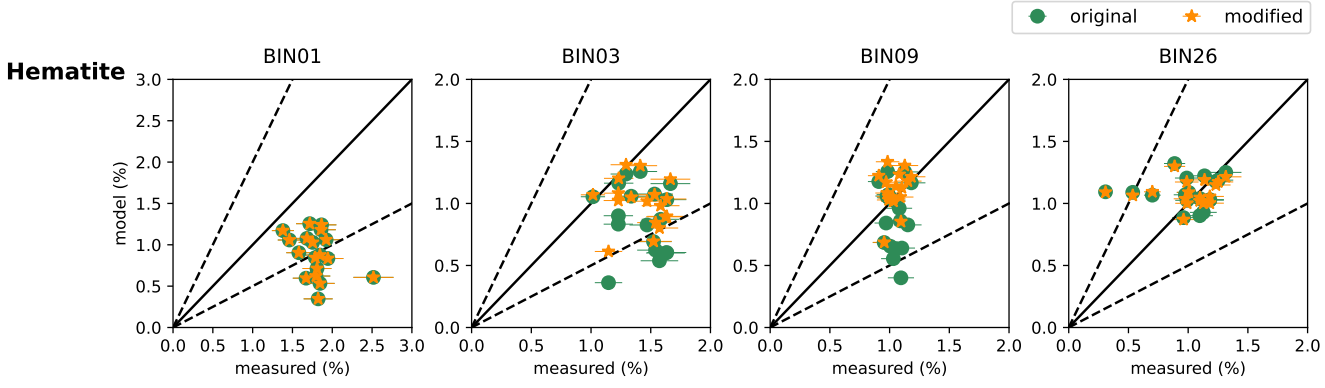

Figure 10. As in Figs.(8& 9) but for hematite by following Eq. 23 replacing $w_{\mathrm{Feox\%}}$ by $w_{\mathrm{Hem\%}}$. Error bars represent 10% variation from the measurement.

Hematite (Fig. 10) is underestimated by an average of 0.9% in BIN01 under both schemes, with the average residuals decreasing at larger sizes. In BIN03, the 'modified' scheme reduces the bias slightly, while in BIN09 and BIN26 the two schemes diverge minimally, yielding both near-zero average residuals (0.1%). On average, hematite increases modestly by 5% in the 'modified' scheme.

Averaged over the JATAC 2022 simulation period, the 'modified' scheme produces substantial increases in phyllosilicates (illite, kaolinite, smectite; +130% relative to the 'original' scheme) and modest changes in hematite (+5%) and calcite (–14%). Conversely, quartz (–61%), feldspar (–56%), and gypsum (–17%) decline substantially. Comparison with measurements shows that the reductions in quartz and feldspar improve model-observation agreement, whereas gypsum agreement deteriorates.

https://doi.org/10.5194/egusphere-2026-23
Preprint. Discussion started: 15 January 2026
© Author(s) 2026. CC BY 4.0 License.

These inter-scheme differences exceed those observed during the DUSTRISK winter simulations, reflecting the seasonal shift in active dust source regions between NH winter and summer (Section 2; Schepanski et al., 2009).

5.3.2 Elemental comparison

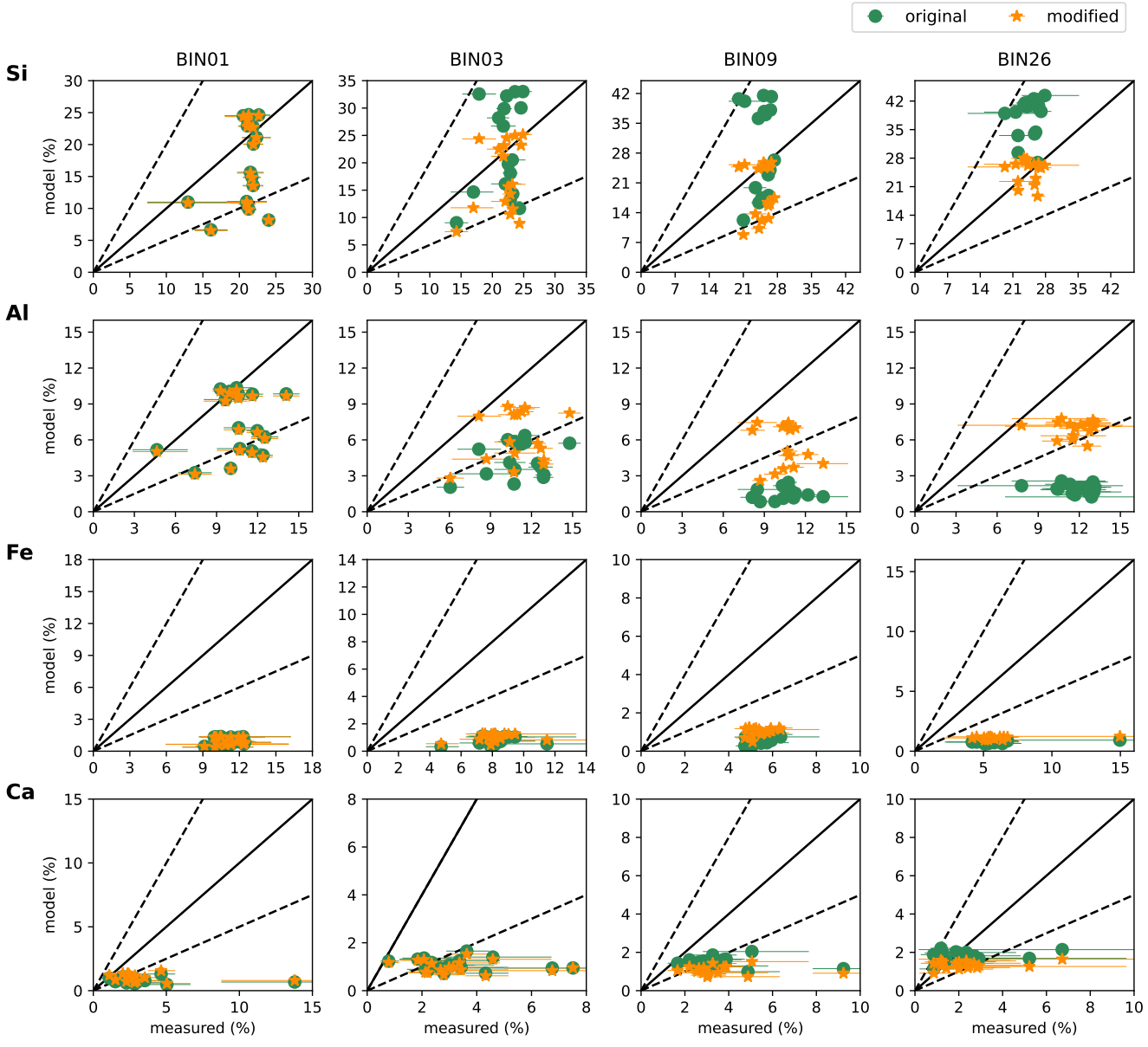

Figure 11. As in Fig. 6 but the titles of the columns are size classifications from COSMO5.05-MUSCAT. The error bars represent the lower and upper limits of the confidence intervals (between 2.5% and 97.5%).

https://doi.org/10.5194/egusphere-2026-23
Preprint. Discussion started: 15 January 2026
© Author(s) 2026. CC BY 4.0 License.

Size-resolved elemental comparisons offer a complementary perspective to the mineral-specific evaluations, enabling accurate assessment of scheme performance. Figure 11 shows comparisons for Si, Al, Fe, and Ca. Silicone content in the finest particles (BIN01) shows minimal differences between schemes. In intermediate sizes (BIN03 and BIN09), the 'modified' scheme transforms model overestimation into underestimation. In the coarsest bin (BIN26), silicone overestimation persists in both schemes but is substantially reduced under the 'modified' approach, with mean residuals improving from +14% to approximately 0%. The silicone improvements trace directly to reduced quartz content in the 'modified' scheme (Fig. 9), confirming that, for some elements, corrections to mineral abundances effectively translate to improved elemental representation.

Aluminum exhibits a clear size-dependent improvement pattern across the bin-resolved analysis. BIN01 shows no significant changes between schemes, while BIN03 reduces underestimation from -7% to -5%, BIN09 improves from -9% to -5%, and BIN26 improves from -10% to -5% in average residuals. This progressive reduction in aluminum underestimation with increasing particle size directly reflects the redistribution of clay minerals into larger size fractions in the 'modified' scheme, a change that better reflects the aggregated nature of phyllosilicates during emission and transport. This feature is also observed in the DUSTRISK elemental comparison for coarser sizes (Fig. 6). Notably, however, the PM2.5 overestimation observed in the DUSTRISK campaign does not appear in this size-resolved analysis, suggesting either biomass burning contamination in the DUSTRISK samples, which would predominantly affect the fine particle fraction, or methodological differences in fine particle measurement between campaigns.

Iron content shows negligible sensitivity to emission scheme choice across all size bins, with severe underestimation in both approaches—a pattern consistent with DUSTRISK (Fig. 6). Notably, the mineral-specific hematite comparison (Fig. 10) also shows no comparable underestimation, exposing a critical discrepancy between mineral and elemental validation metrics. Given iron oxide's pivotal role in dust-atmosphere interactions (Li et al., 2024, 2021; Song et al., 2024; Zhang et al., 2024), this distinction carries significant implications. This inconsistency reveals an inherent limitation of modeling frameworks that treat minerals as discrete particles with uniform composition. Natural atmospheric dust contains iron primarily as nanoscale oxide coatings or inclusions within clay minerals and quartz rather as well as discrete hematite grains (Kandler et al., 2009; Lafon et al., 2004). Neither current model formulations nor available SMAs capture this heterogeneous iron distribution, resulting in systematic biases detectable only through element-resolved evaluations.

Calcium comparison in Fig. 11 exhibits minimal differences between emission schemes across all size bins, consistent with the DUSTRISK results where both schemes substantially underestimate Ca content. Interestingly, for calcium in the bin-resolved comparison, the 'modified' scheme worsens this underestimation, suggesting that the modifications proposed to the mineral size distributions, reduced Ca-bearing minerals beyond what observations support. This systematic Ca deficit aligns with the mineral-specific evaluation, which identified clear underestimation of calcite and gypsum, the dominant Ca-bearing phases in the simulations.

Figure 12 shows the scatterplots for the comparisons between simulated and measured content of K, Mg, and S. Potassium content reveals a complex, size-dependent response to the modifications that varies inconsistently across measurement campaigns. In the bin-resolved analysis, BIN01 shows dramatic improvement under the 'modified' scheme, producing extremely low average mean residuals and substantially reducing the previous underestimations. BIN03 exhibits no significant changes

https://doi.org/10.5194/egusphere-2026-23
Preprint. Discussion started: 15 January 2026
© Author(s) 2026. CC BY 4.0 License.

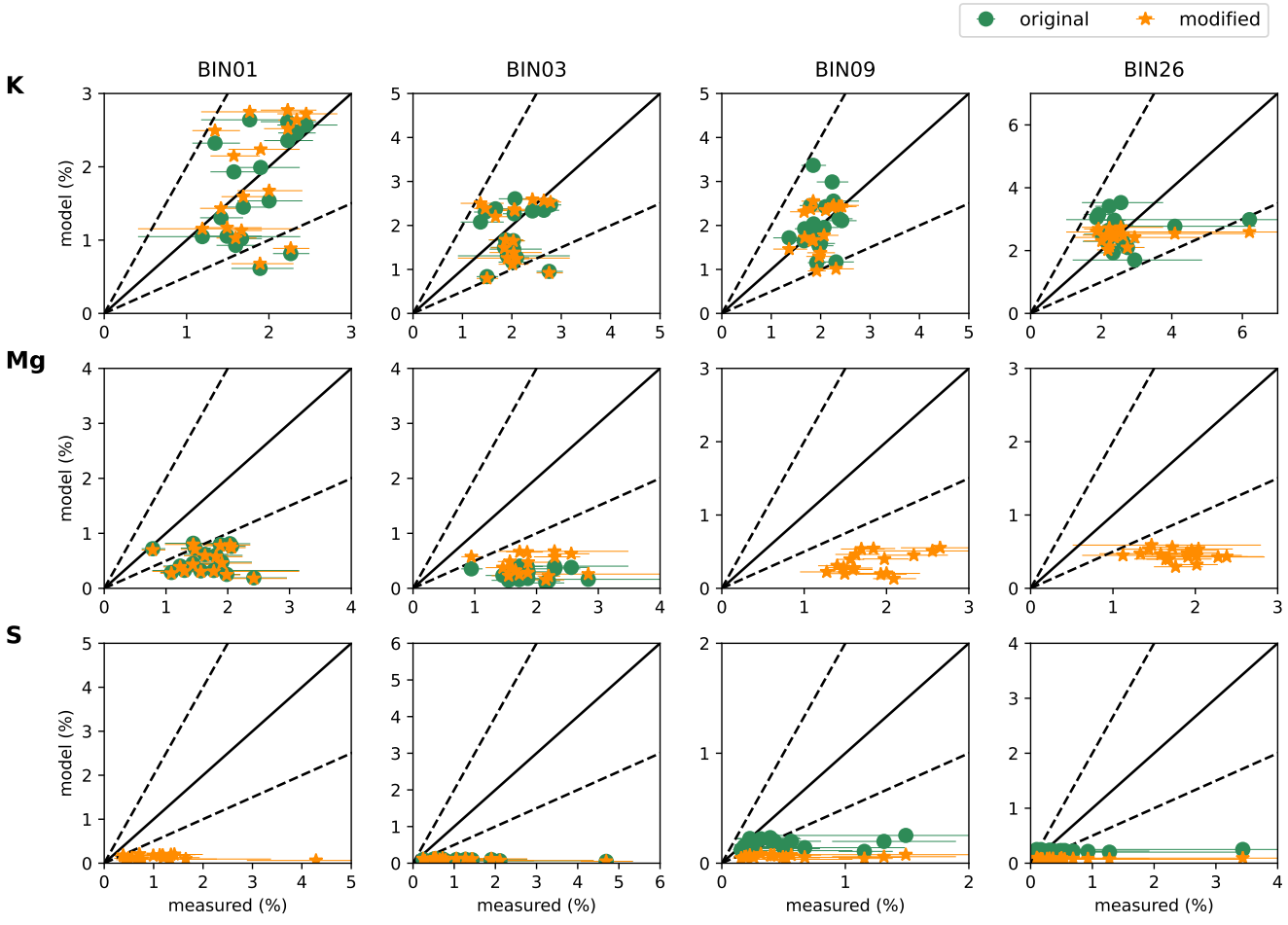

Figure 12. As in Fig. 11 but for K, Mg, and S.

between schemes, while BIN09 transitions from overestimation to underestimation with comparable magnitudes. However, BIN26 demonstrates increased underestimation in the 'modified' scheme. This heterogeneous size-dependent behavior contrasts with the DUSTRISK comparison, where the 'modified' approach yielded improved PM2.5 representation (reducing underestimation from -2% to -1% in mean residuals) but negligible PM10 changes. The mineral-specific feldspar comparison (Fig. 9), meanwhile, showed overall improvement across all sizes for the 'modified' scheme without the pronounced size-dependent variability observed in the elemental K analysis. These inconsistencies across size fractions and measurement campaigns complicate interpretation of the feldspar modifications. K sources and partitioning may be influenced by factors beyond feldspar size distribution adjustments since both illite and feldspar contribute K, making it difficult to isolate their individual influences on elemental K budgets. Furthermore, K contributions from biomass burning or other non-mineral aerosol sources cannot be entirely excluded.

https://doi.org/10.5194/egusphere-2026-23
Preprint. Discussion started: 15 January 2026
© Author(s) 2026. CC BY 4.0 License.

Both emission schemes underestimate magnesium in the size-resolved analysis, with no significant differences between the 'original' and 'modified' approaches. particularly intriguing given that the mineral-specific illite comparison described previously showed dramatic over-representation by the model. This disconnect highlights both the challenges in accurately identifying and quantifying illite in complex mineral assemblages and the prevalence of Mg in silicate aggregates and mixed-mineral phases (Kandler et al., 2018) absent from the model simulation capabilities. DUSTRISK exhibited less severe Mg underestimation, highlighting campaign-dependent model performance variability. Despite this difference, both datasets reveal size-dependent improvements under the 'modified' scheme.

Sulfur is consistently and substantially underestimated by the model across both emission schemes in the bin-resolved comparison, mirroring the systematic underestimation observed in the DUSTRISK dataset. This deficiency directly reflects the earlier gypsum-specific mineral comparison and is attributable to the well-documented underrepresentation of gypsum content in SMAs (Gonçalves Ageitos et al., 2023). The persistent S bias across both measurement campaigns and all size fractions highlights a fundamental limitation in current simulation setups regarding sulfate mineral representation.

In summary, the JATAC 2022 comparison demonstrates that the 'modified' mineralogical scheme improves the representation of quartz, feldspar, and phyllosilicate distributions in COSMO5.05-MUSCAT, while also extending the size range for meaningful model–measurement evaluation. Persistent biases remain for illite, smectite, calcite, and gypsum, reflecting both measurement challenges and uncertainties in source SMAs. Hematite (Fig. 10) shows encouraging agreement in terms of the mineral composition, supporting its robustness for applications sensitive to dust optical properties (e.g., Gómez Maqueo Anaya et al., 2025). However, the systematic elemental Fe underestimation (Fig. 11) reveals that mineral-level validation alone provides an incomplete picture of iron representation, underscoring the importance of complementary elemental constraints.

The comparison between JATAC and DUSTRISK results further reveals the value of multi-campaign evaluation. The JATAC NH summer measurements, conducted within the elevated SAL with minimal biomass burning interference, provide cleaner constraints on mineral dust composition than the NH winter DUSTRISK campaign. Key differences emerge: silicon overestimation in fine particles appears only in DUSTRISK, likely reflecting either the presence of other aerosols or methodological differences; potassium shows campaign-dependent size patterns that highlight the difficulty of attributing elemental K to specific mineral sources; and magnesium underestimation is more pronounced in JATAC despite illite overestimation, exposing limitations in both SMAs, which inadequately represent Mg speciation in mixed silicates, and modeling frameworks that assume single, compositionally uniform mineral particles.

Together, these results highlight both the progress achieved with the 'modified' scheme and the persistent challenges facing mineral dust modeling frameworks. The improvements in quartz and feldspar representation in the model demonstrate that refinements to emission size distributions and mineral abundances can effectively propagate to both mineral and elemental composition. However, the discrepancies in elemental composition for Fe and Mg, combined with campaign-specific variability in model performance, underscore fundamental limitations: current approaches cannot adequately represent the heterogeneous internal mixing of iron and iron oxides, and the complex speciation of magnesium in silicate aggregates. Addressing these limitations will require not only continued refinement of soil mineral assemblage databases and emission parameterizations,

https://doi.org/10.5194/egusphere-2026-23
Preprint. Discussion started: 15 January 2026
© Author(s) 2026. CC BY 4.0 License.

but also expanded observational constraints spanning multiple seasons, source regions, and atmospheric conditions to capture the full complexity of mineral dust composition.

6 Conclusions

The implementation of the 'modified' mineral simulation approach in COSMO5.05-MUSCAT leads to a more accurate representation of dust aerosol composition by adjusting the soil mineralogical database prior to emission flux calculations. Applied to the DUSTRISK 2022 campaign simulation results in comparison with a North African compilation of measurements, the 'modified' scheme substantially improved the representation of phyllosilicates, with kaolinite showing a markedly stronger correlation with observations and illite a slight improvement, though still overestimated. Quartz and feldspar mass fractions decreased significantly, reducing the average quartz residual from 30% to just 1%. Although correlation coefficients for these minerals changed little, the redistribution produced size-resolved fractions that more closely matched observations. Calcite decreased modestly and remained underestimated, while hematite correlations stayed weak, consistent with persistent uncertainties in both its measurement and modeling.

Validation with in-situ *mineral-like* measurements from JATAC 2022 further confirmed these improvements. By redistributing phyllosilicates into larger size bins, the 'modified' scheme improved agreement with measurements in mid-size ranges (BIN03 and BIN09). Quartz residuals dropped substantially across all bins, with overestimation in BIN26 decreasing from 60% to just 11%. Feldspar representation also improved in mid-size bins, while calcite and gypsum remained underestimated in both approaches. Hematite showed similar results across schemes.

The complementary elemental validation for DUSTRISK and JATAC 2022 revealed both the strengths and fundamental limitations of current modeling approaches. In the DUSTRISK 2022 campaign comparisons, several elemental results aligned with their mineral-specific counterparts. For silicon, the 'modified' scheme's substantial reduction in quartz content produced consistent improvements at both scales, with PM2.5 residuals decreasing from +18% to +4% and PM10 from +25% to +15%. Aluminum performance similarly improved in both size fractions, reflecting more accurate size-dependent phyllosilicate distributions. However, systematic iron underestimation persisted in both schemes despite adequate hematite representation at the mineral level. This mineral-element discrepancy exposes a critical modeling limitation: iron exists predominantly as nanoscale oxide coatings or inclusions within other mineral phases (Lafon et al., 2004; Kandler et al., 2007) rather than as discrete particles, a complexity that frameworks treating minerals as single, internally homogeneous particles cannot capture.

The JATAC 2022 size-resolved elemental analysis reinforced these patterns while revealing important inter-campaign differences. Aluminum improvements remained consistent across all size bins but without the fine particle overestimation observed in DUSTRISK, potentially reflecting methodological differences between campaigns. Potassium exhibited campaign-dependent size patterns, underscoring the difficulty of attributing K to specific mineral sources when both feldspar and illite contribute, and the presence of the additional aerosols cannot be completley ruled out. Magnesium underestimation was more pronounced in JATAC despite concurrent illite overestimation, indicating that current soil mineral assemblages cannot adequately represent Mg speciation within mixed silicate aggregates (Kandler et al., 2018). The more severe Mg deficit in JATAC relative to DUS-

https://doi.org/10.5194/egusphere-2026-23
Preprint. Discussion started: 15 January 2026
© Author(s) 2026. CC BY 4.0 License.

TRISK likely reflects reduced biomass burning interference during NH summer SAL sampling rather than improved model performance. These campaign-specific variations demonstrate that model fidelity depends not only on emission parameterizations but also on sampling methodologies and the presence of non-dust aerosol components.

The persistent underestimation of calcite and gypsum additionally highlights ongoing limitations in SMAs and the coarse spatial resolution of regional models, which limits the ability to resolve fine-scale dust source variability. The redistribution of mineral mass fractions, such as >130% increases in phyllosilicates and >50% decreases in quartz and feldspar, illustrates the strong sensitivity of modeled composition to SMA assumptions. These shifts are not only relevant for mineralogical accuracy but also for the radiative, optical, and health-related impacts of dust, emphasizing the importance of continued refinement of mineralogy-specific emission schemes and observational constraints at multiple validation scales.

Taken together, these results demonstrate both progress and remaining challenges in modeling dust mineralogy. The 'modified' scheme clearly improves the size-resolved representation of phyllosilicates, quartz, and feldspar at both mineral and elemental scales, but persistent biases for iron, calcium, and magnesium reveal fundamental limitations in representing the heterogeneous internal mixing and complex speciation characteristic of natural mineral dust. Critically, the elemental validation approach employed here provides a complementary and previously underutilized pathway for model evaluation. By converting simulated mineral compositions to elemental mass fractions and comparing them against measured elemental abundances, this methodology offers several distinct advantages. First, it enables validation against the extensive body of published elemental composition measurements from techniques such as X-ray fluorescence and electron microscopy. Second, it exposes discrepancies between mineral-level and element-level performance that would remain hidden in mineral-only comparisons. Third, it provides independent constraints on mineralogical simulations that can reveal limitations in both emission parameterizations and fundamental assumptions about particle internal structure. The mineral-element discrepancies identified for Fe and Mg exemplify how this dual validation framework diagnoses complexities in dust composition that direct mineral measurements alone cannot adequately capture, underscoring its value for advancing mineralogical representation in atmospheric models.

The seasonal comparison between DUSTRISK (NH winter) and JATAC (NH summer) 2022 further underlines the influence of source region activity. While phyllosilicate increases were consistent across seasons, calcite decreased more strongly in summer (–14%), together with further declines in quartz, feldspar, and gypsum content. These differences reflect shifts in dominant dust-emitting regions and associated meteorology, underscoring the need to account for temporal variability when evaluating mineral fractions in transport models.

Future progress will depend on improved mineralogical datasets, better integration of observations into models, and advances in representing the internal complexity of mineral dust particles. The emergence of hyperspectral measurements from NASA's EMIT mission (Green et al., 2020), alongside field campaigns providing detailed size-resolved composition at both mineral and elemental levels, offers a pathway to reduce current uncertainties. Incorporating such multi-scale observations, particularly for iron oxides and mixed silicate phases, will help resolve biases in key radiatively active minerals and improve constraints on dust–climate interactions. Additionally, developing modeling frameworks that can represent minerals as internally mixed aggregates rather than discrete particles may be necessary to bridge the persistent mineral-element discrepancies identified here.

https://doi.org/10.5194/egusphere-2026-23
Preprint. Discussion started: 15 January 2026
© Author(s) 2026. CC BY 4.0 License.

Recent studies (Li et al., 2021, 2024; Obiso et al., 2024) reinforce that refining soil mineral maps and dust size distributions is critical for advancing our understanding of dust's climatic and biogeochemical roles.

Data availability. The dataset for reproducing the graphs presented here are available at http://doi.org/10.5281/zenodo.18090325

.

Author contributions. SGMA drafted the manuscript. SA, KK, DA, MK, MH, IT, and KS reviewed and edited the manuscript. SGMA, HB, DA, BH, MH, and KS contributed to the conceptualization of the study. SGMA prepared the figures and organized the datasets. EJSS and KWF were responsible for the elemental analysis of samples collected during the DUSTRISK 2022 campaign. SA and KK conducted the elemental analysis and mineral characterization of the samples collected by MK during the JATAC 2022 campaign. MF led the software development by restructuring the code associated with the MUSCAT dust emission scheme. SGMA, MF, BH, KS, and IT contributed to code development related to the inclusion of mineralogy. SGMA, SA, KK, and KS performed the formal data analysis.

Competing interests. The authors declare that they have no conflict of interest

Acknowledgements. This study is done in the framework of the DUSTRISK (a risk index for health effects of mineral dust and associated microbes) project, funded by the Leibniz Collaborative Excellence Programme Project (grant number K255/2019).

This research has been supported by the German Federal Ministry for Economic Affairs and Energy (BMWi) (grant no. 50EE1721C). Furthermore, we also acknowledge the support through ACTRIS-2 under grant agreement no. 654109 from the European Union's Horizon 2020 research and innovation programme and ACTRIS PPP under the Horizon 2020 – Research and Innovation Framework Programme, H2020-INFRADEV- 2016-2017, Grant Agreement number: 7395302.

We acknowledge and thank the team of OSCM / INMG for their crucial and ongoing support. We further thank ESA and the ASKOS/-JATAC teams for the organization of the JATAC(s) campaign(s) and their continuous support.

Further thanks are due to the Deutscher Wetterdienst (DWD) for cooperation and support. We also gratefully acknowledge the Darmstadt Institute for their thorough analysis of the samples, for sharing the results, and for tailoring the analyses to the specific needs of this study. We further thank the National Observatory of Athens for collecting the samples.

Furthermore, ChatGPT was utilized to rephrase and shorten sentences, as well to identify the appropriate prepositions.

https://doi.org/10.5194/egusphere-2026-23
Preprint. Discussion started: 15 January 2026
© Author(s) 2026. CC BY 4.0 License.

References

Adedokun, J. A., Emofurieta, W. O., and Adedeji, O. A.: Physical, mineralogical and chemical properties of harmattan dust at Ile-Ife, Nigeria, Theoretical and Applied Climatology, 40, 161–169, https://doi.org/10.1007/BF00866179, 1989.

Alastuey, A., Querol, X., Castillo, S., Escudero, M., Avila, A., Cuevas, E., Torres, C., Romero, P.-M., Exposito, F., García, O., Pedro Diaz, J., Dingenen, R. V., and Putaud, J. P.: Characterisation of TSP and PM2.5 at Izaña and Sta. Cruz de Tenerife (Canary Islands, Spain) during a Saharan Dust Episode (July 2002), Atmospheric Environment, 39, 4715–4728, https://doi.org/10.1016/j.atmosenv.2005.04.018, 2005.

Albani, S., Mahowald, N. M., Perry, A. T., Scanza, R. A., Zender, C. S., Heavens, N. G., Maggi, V., Kok, J. F., and Otto-Bliesner, B. L.: Improved dust representation in the Community Atmosphere Model, Journal of Advances in Modeling Earth Systems, 6, 541–570, https://doi.org/10.1002/2013MS000279, 2014.

Aryasree, S., Kandler, K., Benker, N., Walser, A., Tipka, A., Dollner, M., Seibert, P., and Weinzierl, B.: Vertical Variability in morphology, chemistry and optical properties of the transported Saharan air layer measured from Cape Verde and the Caribbean, Royal Society Open Science, 11, 231 433, https://doi.org/10.1098/rsos.231433, 2024.

Baldauf, M., Seifert, A., Förstner, J., Majewski, D., Raschendorfer, M., and Reinhardt, T.: Operational Convective-Scale Numerical Weather Prediction with the COSMO Model: Description and Sensitivities, Monthly Weather Review, 139, 3887–3905, https://doi.org/10.1175/MWR-D-10-05013.1, 2011.

Balkanski, Y., Schulz, M., Claquin, T., and Guibert, S.: Reevaluation of Mineral aerosol radiative forcings suggests a better agreement with satellite and AERONET data, Atmospheric Chemistry and Physics, 7, 81–95, https://doi.org/10.5194/acp-7-81-2007, 2007.

Barkan, J., Kutiel, H., Alpert, P., and Kishcha, P.: Synoptics of dust intrusion days from the African continent into the Atlantic Ocean, Journal of Geophysical Research: Atmospheres, 109, 2003JD004 416, https://doi.org/10.1029/2003JD004416, 2004.

Berge, E.: Transboundary air pollution in Europe. Part 2: Numerical addendum to emissions, dispersion and trends of acidifying and eutrophying agents, https://www.osti.gov/etdeweb/biblio/646220, 1997.

Bredeck, G., Dos S. Souza, E. J., Wigmann, C., Fomba, K. W., Herrmann, H., and Schins, R. P.: The influence of long-range transported Saharan dust on the inflammatory potency of ambient PM2.5 and PM10, Environmental Research, 252, 119 008, https://doi.org/10.1016/j.envres.2024.119008, 2024.

Caquineau, S., Gaudichet, A., Gomes, L., Magonthier, M.-C., and Chatenet, B.: Saharan dust: Clay ratio as a relevant tracer to assess the origin of soil-derived aerosols, Geophysical Research Letters, 25, 983–986, https://doi.org/10.1029/98GL00569, 1998.

Chatziparaschos, M., Daskalakis, N., Myriokefalitakis, S., Kalivitis, N., Nenes, A., Gonçalves Ageitos, M., Costa-Surós, M., Pérez García-Pando, C., Zanoli, M., Vrekoussis, M., and Kanakidou, M.: Role of K-feldspar and quartz in global ice nucleation by mineral dust in mixed-phase clouds, Atmospheric Chemistry and Physics, 23, 1785–1801, https://doi.org/10.5194/acp-23-1785-2023, 2023.

Chiapello, I., Bergametti, G., Chatenet, B., Bousquet, P., Dulac, F., and Soares, E. S.: Origins of African dust transported over the northeastern tropical Atlantic, Journal of Geophysical Research: Atmospheres, 102, 13 701–13 709, https://doi.org/10.1029/97JD00259, 1997.

Claquin, T., Schulz, M., and Balkanski, Y.: Modeling the mineralogy of atmospheric dust sources, Journal of Geophysical Research: Atmospheres, 104, 22 243–22 256, https://doi.org/10.1029/1999JD900416, 1999.

Dang, C., Segal-Rozenhaimer, M., Che, H., Zhang, L., Formenti, P., Taylor, J., Dobracki, A., Purdue, S., Wong, P.-S., Nenes, A., Sedlacek III, A., Coe, H., Redemann, J., Zuidema, P., Howell, S., and Haywood, J.: Biomass burning and marine aerosol processing over the southeast Atlantic Ocean: a TEM single-particle analysis, Atmospheric Chemistry and Physics, 22, 9389–9412, https://doi.org/10.5194/acp-22-9389-2022, publisher: Copernicus GmbH, 2022.

https://doi.org/10.5194/egusphere-2026-23
Preprint. Discussion started: 15 January 2026
© Author(s) 2026. CC BY 4.0 License.

Darmenova, K., Sokolik, I. N., Shao, Y., Marticorena, B., and Bergametti, G.: Development of a physically based dust emission module within the Weather Research and Forecasting (WRF) model: Assessment of dust emission parameterizations and input parameters for source regions in Central and East Asia, Journal of Geophysical Research: Atmospheres, 114, https://doi.org/10.1029/2008JD011236, 2009.

Di Biagio, C., Formenti, P., Balkanski, Y., Caponi, L., Cazaunau, M., Pangui, E., Journet, E., Nowak, S., Andreae, M. O., Kandler, K., Saeed, T., Piketh, S., Seibert, D., Williams, E., and Doussin, J.-F.: Complex refractive indices and single-scattering albedo of global dust aerosols in the shortwave spectrum and relationship to size and iron content, Atmospheric Chemistry and Physics, 19, 15 503–15 531, https://doi.org/10.5194/acp-19-15503-2019, 2019.

Di Biagio, C., Balkanski, Y., Albani, S., Boucher, O., and Formenti, P.: Direct Radiative Effect by Mineral Dust Aerosols Constrained by New Microphysical and Spectral Optical Data, Geophysical Research Letters, 47, e2019GL086 186, https://doi.org/10.1029/2019GL086186, 2020.

Enete, I.: Harmattan Dust: Composition, Characteristics and Effects on Soil Fertility in Enugu, Nigeria, British Journal of Applied Science & Technology, 2, 72–81, https://doi.org/10.9734/BJAST/2012/950, 2012.

Engelstaedter, S., Tegen, I., and Washington, R.: North African dust emissions and transport, Earth-Science Reviews, 79, 73–100, https://doi.org/10.1016/j.earscirev.2006.06.004, 2006.

Fomba, K. W., Deabji, N., Barcha, S. E. I., Ouchen, I., Elbaramoussi, E. M., El Moursli, R. C., Harnafi, M., El Hajjaji, S., Mellouki, A., and Herrmann, H.: Application of TXRF in monitoring trace metals in particulate matter and cloud water, Atmospheric Measurement Techniques, 13, 4773–4790, https://doi.org/10.5194/amt-13-4773-2020, 2020.

Formenti, P., Rajot, J. L., Desboeufs, K., Caquineau, S., Chevaillier, S., Nava, S., Gaudichet, A., Journet, E., Triquet, S., Alfaro, S., Chiari, M., Haywood, J., Coe, H., and Highwood, E.: Regional variability of the composition of mineral dust from western Africa: Results from the AMMA SOP0/DABEX and DODO field campaigns, Journal of Geophysical Research: Atmospheres, 113, https://doi.org/10.1029/2008JD009903, _eprint: https://onlinelibrary.wiley.com/doi/pdf/10.1029/2008JD009903, 2008.

Formenti, P., Schütz, L., Balkanski, Y., Desboeufs, K., Ebert, M., Kandler, K., Petzold, A., Scheuvens, D., Weinbruch, S., and Zhang, D.: Recent progress in understanding physical and chemical properties of African and Asian mineral dust, Atmospheric Chemistry and Physics, 11, 8231–8256, https://doi.org/10.5194/acp-11-8231-2011, 2011.

Formenti, P., Caquineau, S., Desboeufs, K., Klaver, A., Chevaillier, S., Journet, E., and Rajot, J. L.: Mapping the physico-chemical properties of mineral dust in western Africa: mineralogical composition, Atmospheric Chemistry and Physics, 14, 10 663–10 686, https://doi.org/10.5194/acp-14-10663-2014, 2014.

Fuster, B., Sánchez-Zapero, J., Camacho, F., García-Santos, V., Verger, A., Lacaze, R., Weiss, M., Baret, F., and Smets, B.: Quality Assessment of PROBA-V LAI, fAPAR and fCOVER Collection 300 m Products of Copernicus Global Land Service, Remote Sensing, 12, 1017, https://doi.org/10.3390/rs12061017, 2020.

Fécan, F., Marticorena, B., and Bergametti, G.: Parametrization of the increase of the aeolian erosion threshold wind friction velocity due to soil moisture for arid and semi-arid areas, Annales Geophysicae, 17, 149–157, https://doi.org/10.1007/s00585-999-0149-7, 1999.

Gebauer, H., Floutsi, A. A., Hofer, J., Haarig, M., Skupin, A., Engelmann, R., Jimenez, C., and Baars, H.: Characterization of the annual cycle of atmospheric aerosol over Mindelo, Cabo Verde, by means of continuous multiwavelength lidar observations, EGUsphere, pp. 1–29, https://doi.org/10.5194/egusphere-2025-3344, publisher: Copernicus GmbH, 2025.

Gonçalves Ageitos, M., Obiso, V., Miller, R. L., Jorba, O., Klose, M., Dawson, M., Balkanski, Y., Perlwitz, J., Basart, S., Di Tomaso, E., Escribano, J., Macchia, F., Montané, G., Mahowald, N. M., Green, R. O., Thompson, D. R., and Pérez García-Pando, C.: Modeling dust

https://doi.org/10.5194/egusphere-2026-23
Preprint. Discussion started: 15 January 2026
© Author(s) 2026. CC BY 4.0 License.

mineralogical composition: sensitivity to soil mineralogy atlases and their expected climate impacts, Atmospheric Chemistry and Physics, 23, 8623–8657, https://doi.org/10.5194/acp-23-8623-2023, 2023.

Green, R. O., Mahowald, N., Ung, C., Thompson, D. R., Bator, L., Bennet, M., Bernas, M., Blackway, N., Bradley, C., Cha, J., Clark, P., Clark, R., Cloud, D., Diaz, E., Ben Dor, E., Duren, R., Eastwood, M., Ehlmann, B. L., Fuentes, L., Ginoux, P., Gross, J., He, Y., Kalashnikova, O., Kert, W., Keymeulen, D., Klimesh, M., Ku, D., Kwong-Fu, H., Liggett, E., Li, L., Lundeen, S., Makowski, M. D., Mazer, A., Miller, R., Mouroulis, P., Oaida, B., Okin, G. S., Ortega, A., Oyake, A., Nguyen, H., Pace, T., Painter, T. H., Pempejian, J., Garcia-Pando, C. P., Pham, T., Phillips, B., Pollock, R., Purcell, R., Realmuto, V., Schoolcraft, J., Sen, A., Shin, S., Shaw, L., Soriano, M., Swayze, G., Thingvold, E., Vaid, A., and Zan, J.: The Earth Surface Mineral Dust Source Investigation: An Earth Science Imaging Spectroscopy Mission, in: 2020 IEEE Aerospace Conference, pp. 1–15, https://doi.org/10.1109/AERO47225.2020.9172731, iSSN: 1095-323X, 2020.

Gómez Maqueo Anaya, S., Althausen, D., Faust, M., Baars, H., Heinold, B., Hofer, J., Tegen, I., Ansmann, A., Engelmann, R., Skupin, A., Heese, B., and Schepanski, K.: The implementation of dust mineralogy in COSMO5.05-MUSCAT, Geoscientific Model Development, 17, 1271–1295, https://doi.org/10.5194/gmd-17-1271-2024, 2024.

Gómez Maqueo Anaya, S., Althausen, D., Hofer, J., Haarig, M., Wandinger, U., Heinold, B., Tegen, I., Faust, M., Baars, H., Ansmann, A., Engelmann, R., Skupin, A., Heese, B., and Schepanski, K.: Investigating the link between mineral dust hematite content and intensive optical properties by means of lidar measurements and aerosol modeling, Atmospheric Chemistry and Physics, 25, 9737–9764, https://doi.org/10.5194/acp-25-9737-2025, 2025.

Gómez Maqueo Anaya, Sofía: Implementation of mineralogical composition of dust aerosol into COSMO-MUSCAT and application to interpret lidar data, Doctoral Dissertation, University of Leipzig, 2025.

Harr, B., Pu, B., and Jin, Q.: The emission, transport, and impacts of the extreme Saharan dust storm of 2015, Atmospheric Chemistry and Physics, 24, 8625–8651, https://doi.org/10.5194/acp-24-8625-2024, 2024.

Harrison, A. D., Lever, K., Sanchez-Marroquin, A., Holden, M. A., Whale, T. F., Tarn, M. D., McQuaid, J. B., and Murray, B. J.: The ice-nucleating ability of quartz immersed in water and its atmospheric importance compared to K-feldspar, Atmospheric Chemistry and Physics, 19, 11 343–11 361, https://doi.org/10.5194/acp-19-11343-2019, 2019.

Heinold, B., Helmert, J., Hellmuth, O., Wolke, R., Ansmann, A., Marticorena, B., Laurent, B., and Tegen, I.: Regional modeling of Saharan dust events using LM-MUSCAT: Model description and case studies, Journal of Geophysical Research: Atmospheres, 112, https://doi.org/10.1029/2006JD007443, _eprint: https://agupubs.onlinelibrary.wiley.com/doi/pdf/10.1029/2006JD007443, 2007.

Heinold, B., Tegen, I., Schepanski, K., Tesche, M., Esselborn, M., Freudenthaler, V., Gross, S., Kandler, K., Knippertz, P., Müller, D., Schladitz, A., Toledano, C., Weinzierl, B., Ansmann, A., Althausen, D., Müller, T., Petzold, A., and Wiedensohler, A.: Regional modelling of Saharan dust and biomass-burning smoke: Part 1: Model description and evaluation, Tellus B: Chemical and Physical Meteorology, 63, 781–799, https://doi.org/10.1111/j.1600-0889.2011.00570.x, 2011.

Huneeus, N., Schulz, M., Balkanski, Y., Griesfeller, J., Prospero, J., Kinne, S., Bauer, S., Boucher, O., Chin, M., Dentener, F., Diehl, T., Easter, R., Fillmore, D., Ghan, S., Ginoux, P., Grini, A., Horowitz, L., Koch, D., Krol, M. C., Landing, W., Liu, X., Mahowald, N., Miller, R., Morcrette, J.-J., Myhre, G., Penner, J., Perlwitz, J., Stier, P., Takemura, T., and Zender, C. S.: Global dust model intercomparison in AeroCom phase I, Atmospheric Chemistry and Physics, 11, 7781–7816, https://doi.org/10.5194/acp-11-7781-2011, 2011.

Iversen, J. D. and White, B. R.: Saltation threshold on Earth, Mars and Venus, Sedimentology, 29, 111–119, https://doi.org/10.1111/j.1365-3091.1982.tb01713.x, 1982.

Jakobsen, H. A., Berge, E., and Jonson, J. E.: The Multi-layer Eulerian Model: Model Description and Evaluation of Transboundary Fluxes of Sulphur and Nitrogen for One Year, DNMI Research Report 49, Meteorological Synthesizing Centre-West, https://books.google.de/

https://doi.org/10.5194/egusphere-2026-23
Preprint. Discussion started: 15 January 2026
© Author(s) 2026. CC BY 4.0 License.

books?id=Lu8ivwEACAAJ, eCE Co-Operative Programme for and Europe, Evaluation of the Long Range Transmission of Air Pollutants in and Meteorological Synthesizing Centre–West (Oslo, Norway), 1997.

Jeong, G. Y. and Achterberg, E. P.: Chemistry and mineralogy of clay minerals in Asian and Saharan dusts and the implications for iron supply to the oceans, Atmospheric Chemistry and Physics, 14, 12 415–12 428, https://doi.org/10.5194/acp-14-12415-2014, 2014.

Journet, E., Balkanski, Y., and Harrison, S. P.: A new data set of soil mineralogy for dust-cycle modeling, Atmospheric Chemistry and Physics, 14, 3801–3816, https://doi.org/10.5194/acp-14-3801-2014, 2014.

Kalu, A.: Saharan Dust Mobilization, Transport, Deposition, chap. The African Dust Plume: Its Characteristics and Propagation across West Africa in Winter, pp. 95–118, John Wiley and Sons, https://scope.dge.carnegiescience.edu/SCOPE_14/SCOPE_14.html, 1979.

Kandler, K., Benker, N., Bundke, U., Cuevas, E., Ebert, M., Knippertz, P., Rodríguez, S., Schütz, L., and Weinbruch, S.: Chemical composition and complex refractive index of Saharan Mineral Dust at Izaña, Tenerife (Spain) derived by electron microscopy, Atmospheric Environment, 41, 8058–8074, https://doi.org/10.1016/j.atmosenv.2007.06.047, 2007.

Kandler, K., Schütz, L., Deutscher, C., Ebert, M., Hofmann, H., Jäckel, S., Jaenicke, R., Knippertz, P., Lieke, K., Massling, A., Petzold, A., Schladitz, A., Weinzierl, B., Wiedensohler, A., Zorn, S., and Weinbruch, S.: Size distribution, mass concentration, chemical and mineralogical composition and derived optical parameters of the boundary layer aerosol at Tinfou, Morocco, during SAMUM 2006, Tellus B: Chemical and Physical Meteorology, 61, 32, https://doi.org/10.1111/j.1600-0889.2008.00385.x, 2009.

Kandler, K., Schütz, L., Jäckel, S., Lieke, K., Emmel, C., Müller-Ebert, D., Ebert, M., Scheuvens, D., Schladitz, A., Šegvić, B., Wiedensohler, A., and Weinbruch, S.: Ground-based off-line aerosol measurements at Praia, Cape Verde, during the Saharan Mineral Dust Experiment: microphysical properties and mineralogy, Tellus B, 63, 459–474, https://doi.org/10.1111/j.1600-0889.2011.00546.x, 2011.

Kandler, K., Schneiders, K., Ebert, M., Hartmann, M., Weinbruch, S., Prass, M., and Pöhlker, C.: Composition and mixing state of atmospheric aerosols determined by electron microscopy: method development and application to aged Saharan dust deposition in the Caribbean boundary layer, Atmospheric Chemistry and Physics, 18, 13 429–13 455, https://doi.org/10.5194/acp-18-13429-2018, 2018.

Kandler, K., Schneiders, K., Heuser, J., Waza, A., Aryasree, S., Althausen, D., Hofer, J., Abdullaev, S. F., and Makhmudov, A. N.: Differences and Similarities of Central Asian, African, and Arctic Dust Composition from a Single Particle Perspective, Atmosphere, 11, 269, https://doi.org/10.3390/atmos11030269, 2020.

Kelly, J. T., Chuang, C. C., and Wexler, A. S.: Influence of dust composition on cloud droplet formation, Atmospheric Environment, 41, 2904–2916, https://doi.org/10.1016/j.atmosenv.2006.12.008, 2007.

Kezoudi, M., Keleshis, C., Antoniou, P., Biskos, G., Bronz, M., Constantinides, C., Desservettaz, M., Gao, R.-S., Girdwood, J., Harnetiaux, J., Kandler, K., Leonidou, A., Liu, Y., Lelieveld, J., Marenco, F., Mihalopoulos, N., Močnik, G., Neitola, K., Paris, J.-D., Pikridas, M., Sarda-Esteve, R., Stopford, C., Unga, F., Vrekoussis, M., and Sciare, J.: The Unmanned Systems Research Laboratory (USRL): A New Facility for UAV-Based Atmospheric Observations, Atmosphere, 12, 1042, https://doi.org/10.3390/atmos12081042, 2021.

Kezoudi, M., Papetta, A., Kandler, K., Ryder, C. L., Leonidou, A., Keleshis, C., Stopford, C., Thornberry, T., Mamouri, R.-E., Sciare, J., and Marenco, F.: Microphysical and Compositional Differences Between Saharan and Middle Eastern Dust Revealed by UAS Observations, https://doi.org/10.5194/egusphere-2025-5234, 2025.

Kinne, S., Schulz, M., Textor, C., Guibert, S., Balkanski, Y., Bauer, S. E., Berntsen, T., Berglen, T. F., Boucher, O., Chin, M., Collins, W., Dentener, F., Diehl, T., Easter, R., Feichter, J., Fillmore, D., Ghan, S., Ginoux, P., Gong, S., Grini, A., Hendricks, J., Herzog, M., Horowitz, L., Isaksen, I., Iversen, T., Kirkevåg, A., Kloster, S., Koch, D., Kristjansson, J. E., Krol, M., Lauer, A., Lamarque, J. F., Lesins, G., Liu, X., Lohmann, U., Montanaro, V., Myhre, G., Penner, J., Pitari, G., Reddy, S., Seland, O., Stier, P., Takemura, T., and Tie, X.: An

https://doi.org/10.5194/egusphere-2026-23
Preprint. Discussion started: 15 January 2026
© Author(s) 2026. CC BY 4.0 License.

AeroCom initial assessment – optical properties in aerosol component modules of global models, Atmospheric Chemistry and Physics, 6, 1815–1834, https://doi.org/10.5194/acp-6-1815-2006, publisher: Copernicus GmbH, 2006.

Kok, J. F.: A scaling theory for the size distribution of emitted dust aerosols suggests climate models underestimate the size of the global dust cycle, Proceedings of the National Academy of Sciences, 108, 1016–1021, https://doi.org/10.1073/pnas.1014798108, 2011.

Kok, J. F., Parteli, E. J. R., Michaels, T. I., and Karam, D. B.: The physics of wind-blown sand and dust, Reports on Progress in Physics, 75, 106 901, https://doi.org/10.1088/0034-4885/75/10/106901, 2012.

Kok, J. F., Storelvmo, T., Karydis, V. A., Adebiyi, A. A., Mahowald, N. M., Evan, A. T., He, C., and Leung, D. M.: Mineral dust aerosol impacts on global climate and climate change, Nature Reviews Earth & Environment, 4, 71–86, https://doi.org/10.1038/s43017-022-00379-5, 2023.

Kumar, A., Abouchami, W., Galer, S. J. G., Singh, S. P., Fomba, K. W., Prospero, J. M., and Andreae, M. O.: Seasonal radiogenic isotopic variability of the African dust outflow to the tropical Atlantic Ocean and across to the Caribbean, Earth and Planetary Science Letters, 487, 94–105, https://doi.org/10.1016/j.epsl.2018.01.025, 2018.

Lafon, S., Rajot, J.-L., Alfaro, S. C., and Gaudichet, A.: Quantification of iron oxides in desert aerosol, Atmospheric Environment, 38, 1211–1218, https://doi.org/10.1016/j.atmosenv.2003.11.006, 2004.

Lawrence, C. R. and Neff, J. C.: The contemporary physical and chemical flux of aeolian dust: A synthesis of direct measurements of dust deposition, Chemical Geology, 267, 46–63, https://doi.org/10.1016/j.chemgeo.2009.02.005, 2009.

Li, L., Mahowald, N. M., Miller, R. L., Pérez García-Pando, C., Klose, M., Hamilton, D. S., Gonçalves Ageitos, M., Ginoux, P., Balkanski, Y., Green, R. O., Kalashnikova, O., Kok, J. F., Obiso, V., Paynter, D., and Thompson, D. R.: Quantifying the range of the dust direct radiative effect due to source mineralogy uncertainty, Atmospheric Chemistry and Physics, 21, 3973–4005, https://doi.org/10.5194/acp-21-3973-2021, 2021.

Li, L., Mahowald, N. M., Gonçalves Ageitos, M., Obiso, V., Miller, R. L., Pérez García-Pando, C., Di Biagio, C., Formenti, P., Brodrick, P. G., Clark, R. N., Green, R. O., Kokaly, R., Swayze, G., and Thompson, D. R.: Improved constraints on hematite refractive index for estimating climatic effects of dust aerosols, Communications Earth & Environment, 5, 295, https://doi.org/10.1038/s43247-024-01441-4, 2024.

Lieke, K., Kandler, K., Scheuvens, D., Emmel, C., Von Glahn, C., Petzold, A., Weinzierl, B., Veira, A., Ebert, M., Weinbruch, S., and Schütz, L.: Particle chemical properties in the vertical column based on aircraft observations in the vicinity of Cape Verde Islands, Tellus B: Chemical and Physical Meteorology, 63, 497, https://doi.org/10.1111/j.1600-0889.2011.00553.x, 2011.

Mahowald, N., Albani, S., Kok, J. F., Engelstaeder, S., Scanza, R., Ward, D. S., and Flanner, M. G.: The size distribution of desert dust aerosols and its impact on the Earth system, Aeolian Research, 15, 53–71, https://doi.org/10.1016/j.aeolia.2013.09.002, 2014.

Marinou, E., Paschou, P., Tsikoudi, I., Tsekeri, A., Daskalopoulou, V., Kouklaki, D., Siomos, N., Spanakis-Misirlis, V., Voudouri, K. A., Georgiou, T., Drakaki, E., Kampouri, A., Papachristopoulou, K., Mavropoulou, I., Mallios, S., Proestakis, E., Gkikas, A., Koutsoupi, I., Raptis, I. P., Kazadzis, S., Baars, H., Floutsi, A., Pirloaga, R., Nemuc, A., Marenco, F., Kezoudi, M., Papetta, A., Močnik, G., Díez, J. Y., Ryder, C. L., Ratcliffe, N., Kandler, K., Sudharaj, A., and Amiridis, V.: An Overview of the ASKOS Campaign in Cabo Verde, in: 16th International Conference on Meteorology, Climatology and Atmospheric Physics—COMECAP 2023, p. 200, MDPI, https://doi.org/10.3390/environsciproc2023026200, 2023.

Marticorena, B. and Bergametti, G.: Modeling the atmospheric dust cycle: 1. Design of a soil-derived dust emission scheme, Journal of Geophysical Research: Atmospheres, 100, 16 415–16 430, https://doi.org/10.1029/95JD00690, 1995.

https://doi.org/10.5194/egusphere-2026-23
Preprint. Discussion started: 15 January 2026
© Author(s) 2026. CC BY 4.0 License.

Miffre, A., Cholleton, D., Noël, C., and Rairoux, P.: Investigating the dependence of mineral dust depolarization on complex refractive index and size with a laboratory polarimeter at 180.0° lidar backscattering angle, Atmospheric Measurement Techniques, 16, 403–417, https://doi.org/10.5194/amt-16-403-2023, 2023.

Miltenberger, A. K., Pfahl, S., and Wernli, H.: An online trajectory module (version 1.0) for the nonhydrostatic numerical weather prediction model COSMO, Geoscientific Model Development, 6, 1989–2004, https://doi.org/10.5194/gmd-6-1989-2013, 2013.

Murray, B. J., O'Sullivan, D., Atkinson, J. D., and Webb, M. E.: Ice nucleation by particles immersed in supercooled cloud droplets, Chemical Society Reviews, 41, 6519, https://doi.org/10.1039/c2cs35200a, 2012.

Muñoz Sabater, J. and Copernicus Climate Change Service, S.: ERA5-Land hourly data from 2001 to present, https://doi.org/10.24381/CDS.E2161BAC, type: dataset, 2019.

Møberg, J., Esu, I., and Malgwi, W.: Characteristics and constituent composition of Harmattan dust falling in Northern Nigeria, Geoderma, 48, 73–81, https://doi.org/10.1016/0016-7061(91)90007-G, 1991.

Nickovic, S., Vukovic, A., Vujadinovic, M., Djurdjevic, V., and Pejanovic, G.: Technical Note: High-resolution mineralogical database of dust-productive soils for atmospheric dust modeling, Atmospheric Chemistry and Physics, 12, 845–855, https://doi.org/10.5194/acp-12-845-2012, 2012.

Obiso, V., Gonçalves Ageitos, M., Pérez García-Pando, C., Perlwitz, J. P., Schuster, G. L., Bauer, S. E., Di Biagio, C., Formenti, P., Tsigaridis, K., and Miller, R. L.: Observationally constrained regional variations of shortwave absorption by iron oxides emphasize the cooling effect of dust, Atmospheric Chemistry and Physics, 24, 5337–5367, https://doi.org/10.5194/acp-24-5337-2024, publisher: Copernicus GmbH, 2024.

Panta, A., Kandler, K., Alastuey, A., González-Flórez, C., González-Romero, A., Klose, M., Querol, X., Reche, C., Yus-Díez, J., and Pérez García-Pando, C.: Insights into the single-particle composition, size, mixing state, and aspect ratio of freshly emitted mineral dust from field measurements in the Moroccan Sahara using electron microscopy, Atmospheric Chemistry and Physics, 23, 3861–3885, https://doi.org/10.5194/acp-23-3861-2023, 2023.

Paris, R., Desboeufs, K. V., Formenti, P., Nava, S., and Chou, C.: Chemical characterisation of iron in dust and biomass burning aerosols during AMMA-SOP0/DABEX: implication for iron solubility, Atmospheric Chemistry and Physics, 10, 4273–4282, https://doi.org/10.5194/acp-10-4273-2010, publisher: Copernicus GmbH, 2010.

Parker, D. J., Burton, R. R., Diongue-Niang, A., Ellis, R. J., Felton, M., Taylor, C. M., Thorncroft, C. D., Bessemoulin, P., and Tompkins, A. M.: The diurnal cycle of the West African monsoon circulation, Quarterly Journal of the Royal Meteorological Society, 131, 2839–2860, https://doi.org/10.1256/qj.04.52, 2005.

Perlwitz, J. P., Pérez García-Pando, C., and Miller, R. L.: Predicting the mineral composition of dust aerosols – Part 1: Representing key processes, Atmospheric Chemistry and Physics, 15, 11 593–11 627, https://doi.org/10.5194/acp-15-11593-2015, 2015a.

Perlwitz, J. P., Pérez García-Pando, C., and Miller, R. L.: Predicting the mineral composition of dust aerosols – Part 2: Model evaluation and identification of key processes with observations, Atmospheric Chemistry and Physics, 15, 11 629–11 652, https://doi.org/10.5194/acp-15-11629-2015, 2015b.

Poggio, L., de Sousa, L. M., Batjes, N. H., Heuvelink, G. B. M., Kempen, B., Ribeiro, E., and Rossiter, D.: SoilGrids 2.0: producing soil information for the globe with quantified spatial uncertainty, SOIL, 7, 217–240, https://doi.org/10.5194/soil-7-217-2021, 2021.

Prigent, C., Aires, F., Rossow, W. B., and Robock, A.: Sensitivity of satellite microwave and infrared observations to soil moisture at a global scale: Relationship of satellite observations to in situ soil moisture measurements, Journal of Geophysical Research: Atmospheres, 110, https://doi.org/10.1029/2004JD005087, 2005.

https://doi.org/10.5194/egusphere-2026-23
Preprint. Discussion started: 15 January 2026
© Author(s) 2026. CC BY 4.0 License.

Pérez García-Pando, C., Miller, R. L., Perlwitz, J. P., Rodríguez, S., and Prospero, J. M.: Predicting the mineral composition of dust aerosols: Insights from elemental composition measured at the Izaña Observatory, Geophysical Research Letters, 43, https://doi.org/10.1002/2016GL069873, 2016.

Rieder, M., Cavazzini, G., D'yakonov, Y. S., Frank-Kamenetskii, V. A., Gottardi, G., Guggenheim, S., Koval', P. W., Müller, G., Neiva, A. M. R., Radoslovich, E. W., Robert, J.-L., Sassi, F. P., Takeda, H., Weiss, Z., and Wones, D. R.: Nomenclature of the Micas, Clays and Clay Minerals, 46, 586–595, https://doi.org/10.1346/CCMN.1998.0460513, 1998.

Rodríguez, S., Calzolai, G., Chiari, M., Nava, S., García, M. I., López-Solano, J., Marrero, C., López-Darias, J., Cuevas, E., Alonso-Pérez, S., Prats, N., Amato, F., Lucarelli, F., and Querol, X.: Rapid changes of dust geochemistry in the Saharan Air Layer linked to sources and meteorology, Atmospheric Environment, 223, 117 186, https://doi.org/10.1016/j.atmosenv.2019.117186, 2020.

Scanza, R. A., Mahowald, N., Ghan, S., Zender, C. S., Kok, J. F., Liu, X., Zhang, Y., and Albani, S.: Modeling dust as component minerals in the Community Atmosphere Model: development of framework and impact on radiative forcing, Atmospheric Chemistry and Physics, 15, 537–561, https://doi.org/10.5194/acp-15-537-2015, 2015.

Schepanski, K., Tegen, I., Laurent, B., Heinold, B., and Macke, A.: A new Saharan dust source activation frequency map derived from MSG-SEVIRI IR-channels, Geophysical Research Letters, 34, https://doi.org/10.1029/2007GL030168, 2007.

Schepanski, K., Tegen, I., and Macke, A.: Saharan dust transport and deposition towards the tropical northern Atlantic, Atmospheric Chemistry and Physics, 9, 1173–1189, https://doi.org/10.5194/acp-9-1173-2009, 2009.

Schepanski, K., Mallet, M., Heinold, B., and Ulrich, M.: North African dust transport toward the western Mediterranean basin: atmospheric controls on dust source activation and transport pathways during June–July 2013, Atmospheric Chemistry and Physics, 16, 14 147–14 168, https://doi.org/10.5194/acp-16-14147-2016, 2016.

Schepanski, K., Heinold, B., and Tegen, I.: Harmattan, Saharan heat low, and West African monsoon circulation: modulations on the Saharan dust outflow towards the North Atlantic, Atmospheric Chemistry and Physics, 17, 10 223–10 243, https://doi.org/10.5194/acp-17-10223-2017, 2017.

Scheuvens, D., Schütz, L., Kandler, K., Ebert, M., and Weinbruch, S.: Bulk composition of northern African dust and its source sediments — A compilation, Earth-Science Reviews, 116, 170–194, https://doi.org/10.1016/j.earscirev.2012.08.005, 2013.

Seinfeld, J. H. and Pandis, S. N.: Atmospheric Chemistry and Physics: From Air Pollution to Climate Change, 3rd Edition \textbar Wiley, John Wiley & Sons, Hoboken, 3 edn., https://www.wiley.com/en-us/Atmospheric+Chemistry+and+Physics%3A+From+Air+Pollution+to+Climate+Change%2C+3rd+Edition-p-9781118947401, 2016.

Shao, Y., Wyrwoll, K.-H., Chappell, A., Huang, J., Lin, Z., McTainsh, G. H., Mikami, M., Tanaka, T. Y., Wang, X., and Yoon, S.: Dust cycle: An emerging core theme in Earth system science, Aeolian Research, 2, 181–204, https://doi.org/10.1016/j.aeolia.2011.02.001, 2011.

Sokolik, I. N. and Toon, O. B.: Incorporation of mineralogical composition into models of the radiative properties of mineral aerosol from UV to IR wavelengths, Journal of Geophysical Research: Atmospheres, 104, 9423–9444, https://doi.org/10.1029/1998JD200048, 1999.

Song, Q., Ginoux, P., Gonçalves Ageitos, M., Miller, R. L., Obiso, V., and Pérez García-Pando, C.: Modeling impacts of dust mineralogy on fast climate response, Atmospheric Chemistry and Physics, 24, 7421–7446, https://doi.org/10.5194/acp-24-7421-2024, publisher: Copernicus GmbH, 2024.

Souza, E. J. D. S., Fomba, K. W., Anaya, S. G. M., Schepanski, K., Freire, S. M., Materić, D., Reemtsma, T., and Herrmann, H.: Particle-bound mercury in Saharan dust-loaded particulate matter in Cabo Verde, Journal of Hazardous Materials, 487, 137 053, https://doi.org/10.1016/j.jhazmat.2024.137053, 2025.

https://doi.org/10.5194/egusphere-2026-23
Preprint. Discussion started: 15 January 2026
© Author(s) 2026. CC BY 4.0 License.

Stein, A. F., Draxler, R. R., Rolph, G. D., Stunder, B. J. B., Cohen, M. D., and Ngan, F.: NOAA's HYSPLIT Atmospheric Transport and Dispersion Modeling System, Bulletin of the American Meteorological Society, 96, 2059–2077, https://doi.org/10.1175/BAMS-D-14-00110.1, publisher: American Meteorological Society Section: Bulletin of the American Meteorological Society, 2015.

Stocker, T. F., Qin, D., Plattner, G.-K., Tignor, M., Allen, S. K., Boschung, J., Nauels, A., Xia, Y., Bex, V., and Midgley, P. M.: Climate Change 2013: The Physical Science Basis, Tech. rep., Intergovernmental Panel on Climate Change, Working Group I Contribution to the IPCC Fifth Assessment Report (AR5)(Cambridge University Press, Cambridge, United Kingdom and New York, NY, USA.), 1535 pp., 2013.

Tegen, I., Harrison, S. P., Kohfeld, K., Prentice, I. C., Coe, M., and Heimann, M.: Impact of vegetation and preferential source areas on global dust aerosol: Results from a model study, Journal of Geophysical Research: Atmospheres, 107, AAC 14–1–AAC 14–27, https://doi.org/10.1029/2001JD000963, 2002.

Tegen, I., Schepanski, K., and Heinold, B.: Comparing two years of Saharan dust source activation obtained by regional modelling and satellite observations, Atmospheric Chemistry and Physics, 13, 2381–2390, https://doi.org/10.5194/acp-13-2381-2013, 2013.

Tesche, M., Gross, S., Ansmann, A., Müller, D., Althausen, D., Freudenthaler, V., and Esselborn, M.: Profiling of Saharan dust and biomass-burning smoke with multiwavelength polarization Raman lidar at Cape Verde, Tellus B: Chemical and Physical Meteorology, 63, 649–676, https://doi.org/10.1111/j.1600-0889.2011.00548.x, 2011.

Wolke, R. and Knoth, O.: Implicit–explicit Runge–Kutta methods applied to atmospheric chemistry-transport modelling, Environmental Modelling & Software, 15, 711–719, https://doi.org/10.1016/S1364-8152(00)00034-7, 2000.

Wolke, R., Schröder, W., Schrödner, R., and Renner, E.: Influence of grid resolution and meteorological forcing on simulated European air quality: A sensitivity study with the modeling system COSMO–MUSCAT, Atmospheric Environment, 53, 110–130, https://doi.org/10.1016/j.atmosenv.2012.02.085, 2012.

Zhang, L., Gong, S., Padro, J., and Barrie, L.: A size-segregated particle dry deposition scheme for an atmospheric aerosol module, Atmospheric Environment, 35, 549–560, https://doi.org/10.1016/S1352-2310(00)00326-5, 2001.

Zhang, X. L., Wu, G. J., Zhang, C. L., Xu, T. L., and Zhou, Q. Q.: What is the real role of iron oxides in the optical properties of dust aerosols?, Atmospheric Chemistry and Physics, 15, 12 159–12 177, https://doi.org/10.5194/acp-15-12159-2015, 2015.

Zhang, Y., Saito, M., Yang, P., Schuster, G., and Trepte, C.: Sensitivities of Spectral Optical Properties of Dust Aerosols to Their Mineralogical and Microphysical Properties, Journal of Geophysical Research: Atmospheres, 129, e2023JD040 181, https://doi.org/10.1029/2023JD040181, 2024.